OPEN ACCESS Freely available online

PLoS PATHOGENS

Quantitative Multicolor Super-Resolution Microscopy Reveals Tetherin HIV-1 Interaction

Martin Lehmann[1], Susana Rocha[2], Bastien Mangeat[1,3], Fabien Blanchet[3], Hiroshi Uji-i[2], Johan Hofkens[2], Vincent Piguet[1,3]*

1 Departments of Microbiology and Molecular Medicine, Dermatology and Venereology, University Hospital and Medical School of Geneva, Geneva, Switzerland, **2** Laboratory for Photochemistry and Spectroscopy, Department of Chemistry, Katholieke Universiteit Leuven, Heverlee, Belgium, **3** Department of Dermatology and Wound Healing, Cardiff University School of Medicine and University Hospital of Wales, Cardiff, Wales, United Kingdom

Abstract

Virus assembly and interaction with host-cell proteins occur at length scales below the diffraction limit of visible light. Novel super-resolution microscopy techniques achieve nanometer resolution of fluorescently labeled molecules. The cellular restriction factor tetherin (also known as CD317, BST-2 or HM1.24) inhibits the release of human immunodeficiency virus 1 (HIV-1) through direct incorporation into viral membranes and is counteracted by the HIV-1 protein Vpu. For super-resolution analysis of HIV-1 and tetherin interactions, we established fluorescence labeling of HIV-1 proteins and tetherin that preserved HIV-1 particle formation and Vpu-dependent restriction, respectively. Multicolor super-resolution microscopy revealed important structural features of individual HIV-1 virions, virus assembly sites and their interaction with tetherin at the plasma membrane. Tetherin localization to micro-domains was dependent on both tetherin membrane anchors. Tetherin clusters containing on average 4 to 7 tetherin dimers were visualized at HIV-1 assembly sites. Combined biochemical and super-resolution analysis revealed that extended tetherin dimers incorporate both N-termini into assembling virus particles and restrict HIV-1 release. Neither tetherin domains nor HIV-1 assembly sites showed enrichment of the raft marker GM1. Together, our super-resolution microscopy analysis of HIV-1 interactions with tetherin provides new insights into the mechanism of tetherin-mediated HIV-1 restriction and paves the way for future studies of virus-host interactions.

Citation: Lehmann M, Rocha S, Mangeat B, Blanchet F, Uji-i H, et al. (2011) Quantitative Multicolor Super-Resolution Microscopy Reveals Tetherin HIV-1 Interaction. PLoS Pathog 7(12): e1002456. doi:10.1371/journal.ppat.1002456

Editor: Hans-Georg Krausslich, Universitätsklinikum Heidelberg, Germany

Received May 17, 2011; **Accepted** November 9, 2011; **Published** December 15, 2011

Funding: VP was supported by the Human Science Frontier Program and Swiss National Science Foundation. SR was supported by Portuguese Foundation for Science and Technology (FCT) PhD grant SFRH/BD/27265/2006. JH was supported by the long-term structural funding program "Methusalem" by the Flemish government, the K.U. Leuven research fund (GOA 2006/2, CREA2007), Fonds voor Wetenschappelijk Onderzoek Vlaanderen (FWO grant G.0402.09) and the Herculesstichting. The funders had no role in study design, data collection and analysis, decision to publish, or preparation of the manuscript.

Competing Interests: The authors have declared that no competing interests exist.

* E-mail: piguetv@cardiff.ac.uk

Introduction

Although viruses heavily depend on the host cell machinery for their replication, they also face numerous blockades imposed by cellular proteins at several distinct steps in their life cycle. Recently, tetherin, an interferon-induced transmembrane protein has been shown to restrict the release of HIV-1 [1,2] and other enveloped viruses [3–5]. Viruses also possess several anti-tetherin activities encoded by proteins such as HIV-1 Vpu [2,6], SIV Nefs and Envelope (ENV) [7–9], HIV-2 ENV[10] and Karposi's sarcoma-associated herpesvirus K5 [5].

Tetherin possesses two membrane anchors in an unusual topology, namely a N-terminal transmembrane (TM) domain and a C-terminal glycophosphatidylinositol (GPI) lipid anchor, proposed to mediate lipid raft interaction [11]. The extracellular domains of two tetherin molecules form parallel cysteine-linked coiled-coil domains [12,13]. Perez-Caballero *et al.* used tetherin mutants and artificial tetherin composed of fragments of heterologous proteins in a tetherin-like topology to demonstrate that tetherin inhibits HIV-1 release through direct tethering of virions to cells [13]. Direct incorporation of tetherin into HIV-1 virions was also confirmed by biochemical analysis and electron microscopy [13–15]. HIV-1 Vpu interacts with the tetherin transmembrane domain [6,16] and counteracts tetherin by degradation and removal from the cell surface [2,17–19]. Through these combined activities, Vpu impairs incorporation of tetherin into virions and restriction [13]. Detailed analysis of tetherin distribution in the plasma membrane, of the role of lipid rafts in HIV-1 tetherin interactions and of the orientation and number of tetherin molecules involved in restriction is still lacking.

HIV-1 assembly into virions of 100–150 nm diameter at the plasma membrane of infected cells involves an extensive range of host cell factors [20]. Widely used electron microscopy techniques provide detailed pictures of viral and cellular structures, but high density labeling of viral and cellular proteins as well as quantitative image analysis remain challenging. Novel single-molecule super-resolution imaging by photoactivated localization microscopy (PALM) [21], fluorescence PALM (fPALM) [22], stochastic optical reconstruction microscopy (STORM) [23] and direct STORM (dSTORM) [24] exploit photoswitching properties of photoactivatable fluorescent proteins (PAFP) and organic dyes to localize them with nanometer resolution. Multicolor super-resolution microscopy [25,26] can resolve distances of 20–200 nm that are relevant for virus-host interactions and bridge the gap between

Author Summary

Human immunodeficiency virus 1 (HIV-1) assembles and interacts with cellular proteins at the plasma membrane of infected cells. Here, we analyzed individual HIV-1 virions, viral assembly sites and the mechanism of tetherin restriction by multicolor super-resolution microscopy using fully functional fluorescently labeled tetherin and viral proteins. Viral proteins within virions were visualized with nanometer resolution yielding new insight into the structure of the HIV-1. Our super-resolution analysis was extended to tetherin, a cellular restriction factor that inhibits the release of several enveloped viruses. Tetherin was localized in clusters of 70–90 nm at the plasma membrane that contain 5–11 dimers. In contrast tetherin clusters found at HIV-1 assembly sites contained on average 4–7 tetherin dimers. Clustering of tetherin was dependent on both tetherin membrane anchors. The transmembrane domain of tetherin associated with budding virions independently of GM1 lipid raft domains. Our data indicated that extended dimers tether HIV-1 virions directly to the cell. Overall, we provide for the first time super-resolution analysis of authentic virions, virus budding sites and HIV-1 interactions with the anti-viral factor tetherin. Our data offer novel insights into the mechanisms of tetherin restriction.

Fluorescence Resonance Energy transfer (FRET) and conventional diffraction limited fluorescence microscopy [27].

Previous super-resolution imaging revealed single molecule dynamics and assembly of tandem-EosFP tagged HIV-1 Gag into virus-like particles of 100–200 nm [21,28].

Here, we set up labeling of HIV-1 and tetherin with monomeric PAFP and antibody staining for multicolor super-resolution microscopy in cells. We visualized precise localization of HIV-1 proteins in virions and at budding sites at the plasma membrane of cells. Super-resolution analysis showed that tetherin formed clusters, whose integrity depended on both membrane anchors. Importantly, tetherin clusters closely associated with HIV-1 budding sites. Through a combination of biochemical analysis and super-resolution microscopy of tetherin mutants, we showed that tetherin restricts virion release as extended dimers and that the transmembrane domain of tetherin possesses affinity for HIV-1 assembly sites.

Results

In order to perform single-molecule super-resolution microscopy of HIV-1, we fused different PAFP to HIV-1 Gag, the major structural protein of virions, yielding: Gag-Dronpa, Gag-PS-CFP2, Gag-Dendra2, Gag-mKikGR, Gag-mEosFP and Gag-PAmCherry (Figure S1A). The monomeric PAFP are expected to minimally interfere with HIV-1 particle formation [29,30], a potential caveat of the Gag fused to tandem-EosFP. The different constructs were expressed together with full-length HIV-1 in 293T cells and analyzed for incorporation into HIV-1 particles, effect on viral infectivity and performance in single-color super-resolution imaging [31]. We selected Gag-Dronpa and Gag-mEosFP for super-resolution imaging of HIV-1 virions, due to their expression as full length fusion proteins, minimal impact on infectivity and superior signal-to-noise ratios (Figure S1B–D).

To visualize HIV-1 and cellular proteins labeled with PAFP or Alexa Fluor 647 labeled antibodies, we setup a two-color super-resolution microscope with widefield illumination in total internal reflection (TIR) mode. Fluorescence emission of Dronpa, mEosFP and Alexa Fluor 647 were detected simultaneously by two Electron Multiplying CCD cameras using specific filter sets and synchronized photoactivation/excitation/detection schemes as depicted in Figure S2. Notably, differences in alignment of both cameras and chromatic aberrations were corrected using a high resolution mapping procedure (Figure S3) based on local weighted mean transformation [32]. Colocalization precision of $\sim$17 nm throughout the total field of view was routinely achieved (Figure S3F). Our two-color super-resolution microscope therefore enabled colocalization analysis of proteins labeled with PAFP or antibodies in the range of 20–200 nm which covers scales relevant to HIV-1 host interactions.

HIV-1 virion structure and assembly sites

To determine the localization of HIV-1 proteins within virions, we performed super-resolution microscopy on double-labeled HIV-1 particles.

HIV-1 virions specifically incorporated Dronpa-labeled Vpr, a HIV-1 protein associated with viral cores, Gag-Dronpa and Gag-mEosFP, but not Dronpa alone (Figure 1A and Figure S4A). Notably, labeling HIV-1 virions with the monomeric PAFP fusions minimally affected infectivity and therefore likely preserves virion structure (Figure 1B).

HIV-1 virions that contained HA-tagged integrase (INHA) and Dronpa-Vpr were fixed on coverslips, permeabilized and further labeled by indirect immunofluorescence against Integrase (IN), capsid (CA), matrix (MA) or gp120 envelope (ENV) followed by Alexa Fluor 647-coupled secondary antibodies (Figure 1C–E). Super-resolution microscopy of double labeled virus particles showed an important increase in resolution when compared to diffraction-limited confocal laser scanning or total internal reflection fluorescence (TIRF) microscopy (Figure 1C and Figure S1D). The high degree of colocalization in super-resolution images of the two HIV-1 proteins Dronpa-Vpr and CA (Figure 1C) demonstrated the performance of the calibration procedure in a biological context. The sizes of HIV-1 structures were determined through cluster analysis of single molecule localizations as described in Materials and Methods after testing on simulated clusters (Figure S5). We found similar average sizes for Dronpa-Vpr (94$\pm$17 nm), Gag-Dronpa (108$\pm$39 nm) and Gag-mEosFP (94$\pm$37 nm, mean$\pm$StD) consistent with their localization inside HIV-1 virions (Figure S4B).

In contrast, IN, CA, MA and ENV showed more variable sizes: 75$\pm$20 nm for IN, 112$\pm$31 nm for CA, 117$\pm$45 nm for MA and 127$\pm$45 nm for ENV (mean$\pm$StD, Figure 1D and Figure S4C). Notably, IN colocalized with Dronpa–Vpr cores as a discrete structure with narrow size distributions, likely due to their common presence in the viral core. Similar sizes observed for CA and MA structures could result from proximity of the C-terminal epitope of mature MA and the epitope recognized by the CA antibody. In contrast, HIV-1 ENV was found in 1-2 discrete peripheral clusters per Dronpa-Vpr containing virion (Figure 1E).

Next, we used super-resolution microscopy to visualize HIV-1 in a cellular context. We analyzed HIV-1 protein distribution at the plasma membrane of non-permeabilized HeLa cells transfected with HIV-1 and Gag-mEosFP and stained for ENV. We observed distinct clusters of Gag-mEosFP surrounded by antibody labeled ENV clusters (Figure 1F) that represent HIV-1 assembly sites [21,28,29]. Altogether, our data demonstrates that super-resolution microscopy allows precise localization of HIV-1 proteins in infectious virions and budding structures, which previously could only be observed by electron microscopy [33–35].

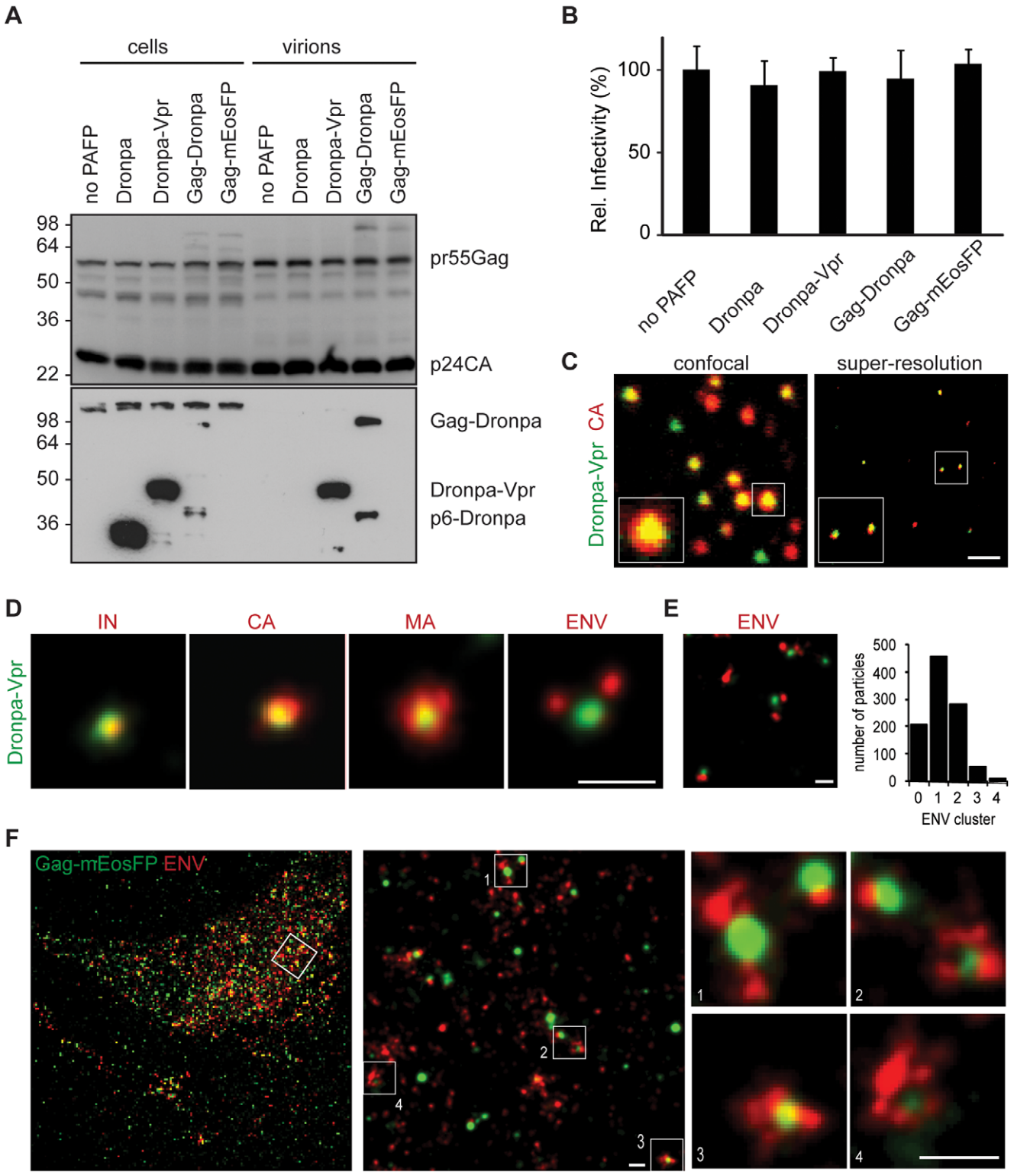

Figure 1. Structural features of single HIV-1 virions and assembly sites are revealed by multicolor super-resolution microscopy. (A) Western blot analysis (anti-p24CA upper, anti-Dronpa bottom) of cellular lysates and purified virions from 293T cells transfected with HIV-1 INHA and indicated photoactivatable fluorescent protein (PAFP). Sizes of molecular weight markers are shown in kilodaltons. (B) Relative infectivity of virions from (A). Error bars represent standard deviation of triplicate titrations. One representative experiment out of two is shown for panel A and B. (C) Virions labeled with Dronpa-Vpr and primary anti-CA and Alexa Fluor 647 secondary antibodies were analyzed by confocal laser scanning (left) or super-resolution microscopy (right). (D) Virions containing Dronpa-Vpr (green) were labeled by indirect immunofluorescence with primary antibodies against HA (IN), HIV-1 capsid (CA), matrix (MA) or gp120 (ENV) and Alexa Fluor 647 secondary antibodies (red). Representative super-resolution images from two virus preparations are shown. (E) Super-resolution image (left) of ENV (red) on Dronpa-Vpr particles (green). Quantification (right) was performed by counting the number of ENV clusters on 1000 HIV-1 particles in 4 images of two independent virus preparation. (F) HeLa cells

expressing HIV-1 Δvpu and Gag-mEosFP (green) were labeled by indirect immunofluorescence with primary anti-gp120 (ENV) and Alexa Fluor 647 secondary antibodies (red), conventional resolution (left) and super-resolution image (right), scale bars 1 μm (c) and 200 nm (d–f).
doi:10.1371/journal.ppat.1002456.g001

Tetherin distribution and orientation

We next set out to visualize HIV-1 tetherin interactions at the plasma membrane using this technique. First, the plasma membrane distribution of endogenous and overexpressed tetherin was analyzed by super-resolution microscopy in cells. Tetherin constructs containing N-terminal mEosFP or epitope-tags (HA or Flag) inserted after the extracellular coiled-coil domain (Figure 2A) efficiently restricted the release of vpu-deficient HIV-1 (HIV-1 Δvpu) and are counteracted by Vpu in transfected 293T cells (Figure 2B and Figure S6A). Notably the cellular levels of mEosFP-tetherin, tetherin-Flag and tetherin-HA were reduced in presence of HIV-1 Vpu (Figure 2C and Figure S6B), indicating efficient Vpu-mediated degradation of these constructs. The N-terminal fusion of mEosFP to tetherin does not interfere with HIV-1 assembly (Figure S6C) and no cleavage of the fusion protein was observed (Figure 2C and Figure S6C). Overall, labeling tetherin with PAFP and epitope-tags minimally affects restriction activity and preserves Vpu-sensitivity.

In HeLa cells we found endogenous and overexpressed tetherin in homogenously distributed clusters of 70–90 nm using labeling with mEosFP or antibody staining followed by super-resolution microscopy (Figure 2D). Ripley's L function was previously used to characterize extent of clustering of influenza hemagglutinin (HA) and T cell receptor complexes [36,37] and was tested on simulated clusters of 50–400 nm (Figure S5). Ripley's L function indicated clustering of endogenous tetherin and all tetherin constructs tested (Figure 2E). In contrast tetherin mutants lacking the transmembrane domain (delTM) or GPI anchor (delGPI) showed decreased clustering (Figure 2F), which was confirmed by decreased peaks of Ripley's L function that shifted to larger distances compared to wild-type tetherin (Figure 2G). Overall, labeling of tetherin for super-resolution microscopy preserved restriction activity, Vpu-sensitivity and revealed a clustered distribution, which depends on both tetherin's membrane anchors.

Distribution of tetherin molecules at HIV-1 assembly sites

Since super-resolution microscopy enabled us to resolve structural features of viral particles and the distribution of tetherin (Figures 1 and 2), we next determined where tetherin localizes with respect to HIV-1 assembly sites. HeLa cells were cotransfected with HIV-1 Δvpu and Gag-mEosFP and tetherin-HA or tetherin-Flag and analyzed by indirect immunofluorescence and super-resolution microscopy. Gag-mEosFP-containing budding structures at the plasma membrane were mostly found in close proximity with a single cluster of tetherin-HA or tetherin-Flag (Figure 3A and B). Similarly, mEosFP-tetherin clusters were found close to groups of HIV-1 ENV clusters at HIV-1 assembly sites (Figure 3C). Close examination of 500 individual tetherin-positive budding sites revealed that 80% contained a single cluster of mEosFP-tetherin (Figure S6D). Finally bivariant Ripley's L function confirmed coclustering of different tetherin constructs with either Gag-mEosFP or HIV-1 ENV at HIV-1 budding sites (Figure 3D). We conclude that tetherin in single clusters closely associates with HIV-1 budding sites.

Tetherin restriction mechanism

As both tetherin membrane anchors are essential for restricting HIV-1 release [13], different orientations of tetherin dimers across the cell and viral membrane are possible. Two models must be considered: (i) the "extended model" in which pairs of membrane anchors are incorporated into the cell membrane and the viral membrane, and an extended coiled-coil domain spans the gap between both membranes or (ii) the "parallel model" where one tetherin monomer is incorporated into the cell membrane and the other monomer into the viral membrane (Figure 4A). The apparent distances of circa 17 nm found between tethered virions by electron microscopy [6] and the structure of the tetherin ectodomain [12] favor the extended model but definitive proof is missing.

Tetherin-restricted virions are efficiently released from the cell surface by treatment with subtilisin A, a protease with relatively low specificity [1,6,14,15]. If virions are retained following the parallel model, subtilisin A treatment should leave monomeric low molecular weight N-termini inside stripped particles.

293T cells expressing HIV-1 Δvpu and N-terminal HA-tagged tetherin were treated with subtilisin A, cell lysates and released virions were then analyzed by Western blot. Analysis of cellular extracts showed constant pr55Gag content, whereas the majority of glycosylated tetherin at 36 and 60 kDa, as well as virions containing p24CA were efficiently removed by subtilisin A treatment (Figure 4B). Only a HA fragment of ~26 kDa was found inside stripped virions by non-reducing SDS-PAGE/Western blot analysis (Figure 4B). Under reducing SDS-PAGE a single band migrated at ~13 kDa, consistent with a previously proposed cleavage site at RNVT/H68 [13,14]. Altogether, we found dimeric N-termini associated with subtilisin A stripped virions, which is not compatible with the parallel model of tetherin orientation.

If tetherin retains viruses via the extended model, cleavage of the tetherin GPI anchor by phosphatidyl-inositol-specific phospholipase C (PI-PLC) should release tethered virions. To test this hypothesis, 293T cells transfected with HIV-1 Δvpu and tetherin-HA, HA-tetherin or the inactive mutant tetherin-HA delTM (Figure S6A and [13]) were treated with PI-PLC or subtilisin A. Stripped virions were pelleted through sucrose and analyzed by Western blot. Both PI-PLC and subtilisin A treatment released virions retained by tetherin (Figure 4C). Quantification from several experiments revealed that PI-PLC treatment (1 U/ML) released 20% of virions compared to the maximal release by 5 μg/ML subtilisin A (Figure 4D). To compare PIPLC and subtilisin A activities on tetherin we used wt tetherin HA and the mutant delTM, that is attached to the cell only via a GPI anchor. Fluorescence-activated cell sorting (FACS) analysis revealed that PI-PLC specifically reduced cell-surface levels of tetherin-HA delTM, whereas increased signal from tetherin-HA could result from increased access of antibodies to the internal HA tag after tetherin GPI cleavage (Figure 4E). Subtilisin A treatment removed the majority of tetherins from the cell surface, indicating that lower release of tetherin restricted virions by PI-PLC can be explained by its lower activity in cleaving the tetherin GPI anchor when compared to proteolysis cleavage by subtilisin A.

Finally, virions released by PI-PLC treatment contained nearly full length dimeric tetherin (Figure 4F). Therefore, since both PI-PLC and subtilisin A treatments removed tethered virions, which respectively contained dimeric tetherin and dimeric N-terminal tetherin fragments we conclude that tetherin restricts HIV-1 release as an extended dimer.

To characterize further the orientation of tetherin upon incorporation into the membrane of assembling virions, we

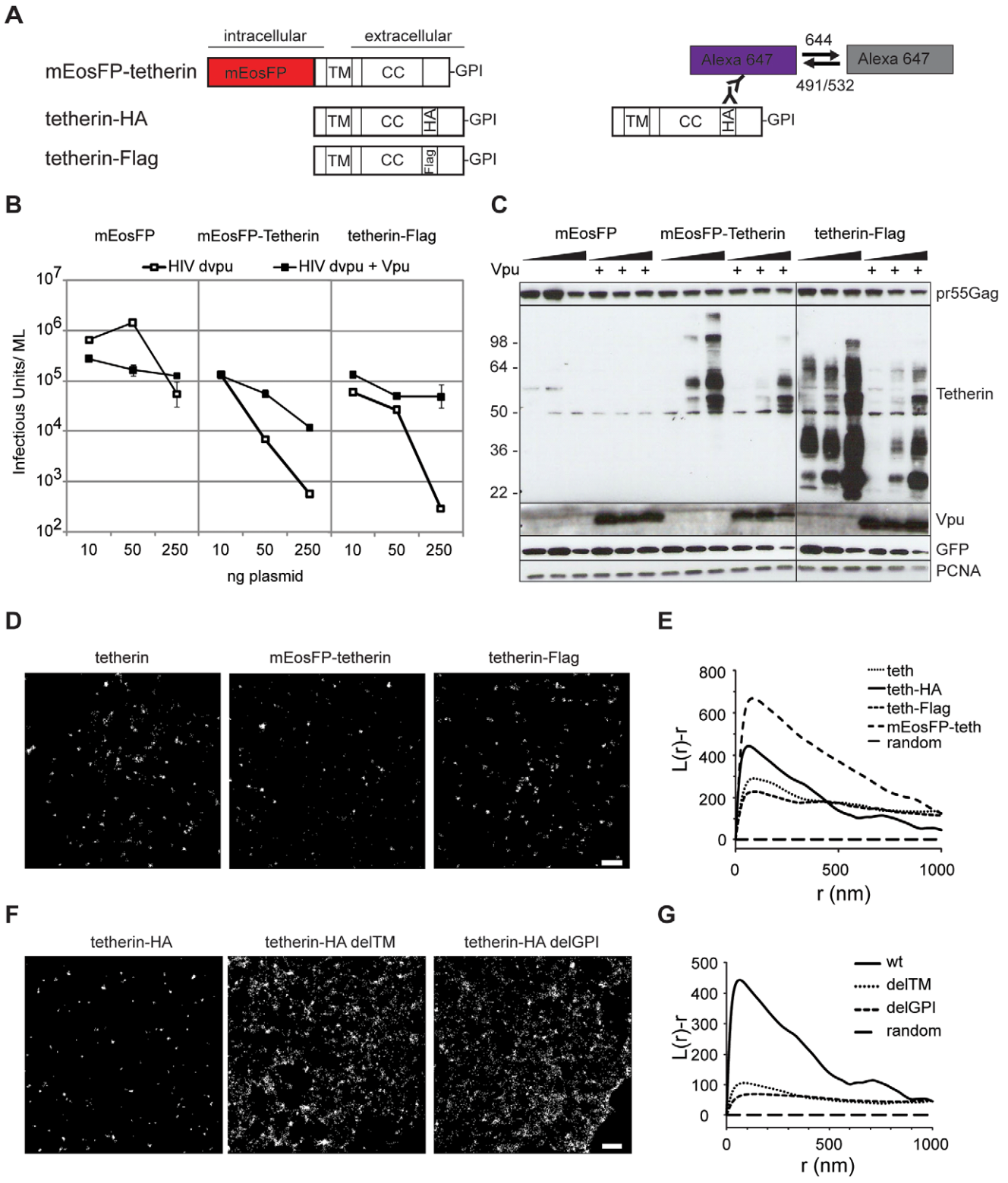

Figure 2. Tetherin localization to micro-domains depends on both membrane anchors. (A) Schematic presentation of tetherin constructs used and labeling/photoswitching scheme of fluorescent Alexa Fluor 647 (violet) and dark state (grey), tetherin structural features are: transmembrane domain (TM), coiled-coil domain (CC) and Glycosylphosphatidylinositol (GPI) anchor. HA or Flag are internal HA or Flag tags. (B) 293T cells were transfected with HIV-1 Δvpu and either mEosFP, mEosFP-tetherin or tetherin-Flag without or with Vpu as indicated and infectious output was determined on HeLa indicator cells. Error bars represent range of duplicate titrations. (C) Western blot analysis of cell lysates from B) was performed for pr55Gag, tetherin, Vpu, GFP as transfection control and PCNA as loading control. Sizes of molecular weight markers are shown in kilodaltons. One representative experiment out of two is shown for panel B and C. (D) Representative regions of super-resolution images of HeLa cells expressing HIV-1 Δvpu and empty plasmid, mEosFP-tetherin or tetherin-Flag that were labeled by indirect immunofluorescence against tetherin or

Flag or left unlabeled (mEosFP-tetherin), scale bar 500 nm. E) Ripley's L analysis: normalized L(r)-r plots indicate clustering at distances r with positive L(r)-r values, F) Representative regions of super-resolution images of HeLa cells expressing HIV-1 Δvpu and indicated tetherin-HA or mutant constructs. The cells were labeled by indirect immunofluorescence with primary anti-HA and Alexa Fluor 647 secondary antibodies, scale bar 500 nm. G) Ripley's L analysis indicates higher degree of clustering of wt tetherin than tetherin mutants delTM and delGPI.
doi:10.1371/journal.ppat.1002456.g002

analyzed the distribution of tetherin mutants lacking one of the membrane anchors relative to HIV-1 budding sites by super-resolution microscopy and co cluster analysis using bivariant Ripley's L function. HeLa cells were transfected with HIV-1 Δvpu, Gag-mEosFP and tetherin-HA or its mutants delTM and delGPI and labeled by anti-HA immunofluorescence. Tetherin-HA and the delGPI mutant, but not delTM associated with Gag-mEosFP-containing budding sites (Figure 5), indicating that the tetherin transmembrane domain drives tetherin localization to HIV-1 budding sites.

Finally to test whether tetherin could associate with budding structures via lipid rafts, HeLa cells expressing HIV-1 Δvpu and Gag-mEosFP or mEosFP-tetherin, were fixed, stained for the lipid raft marker GM1 using Alexa Fluor 647 Cholera-toxin and analyzed by super-resolution microscopy and co cluster analysis using bivariant Ripley's L function. GM1 localized to clusters of variable sizes that showed minor coclustering with mEosFP-tetherin domains, but did not show significant overlap (Figure 6B and C), indicating that both proteins are found in distinct, but adjacent domains. In contrast, we could not detect significant coclustering of GM1 with Gag-mEosFP-containing HIV-1 budding sites (Figure 6A and C). As positive control for coclustering, we monitored mEosFP-tetherin and tetherin-HA at HIV-1 budding sites labeled by HIV-1 ENV and Gag-mEosFP, respectively (Figure 3D and 6C). In addition, the GPI anchor was not sufficient to mediate enrichment of tetherin-HA delTM at budding sites (Figure 5). We conclude that tetherin and GM1, although both were reported to associate with lipid rafts, localize to different but adjacent lipid domains and that GM1-containing lipid rafts and the tetherin GPI anchor are unlikely to drive tetherin to HIV-1 assembly sites.

Quantification of tetherin molecules at HIV-1 assembly sites

Single-molecule imaging and localization of PAFP provides super-resolution images and was previously used to estimate

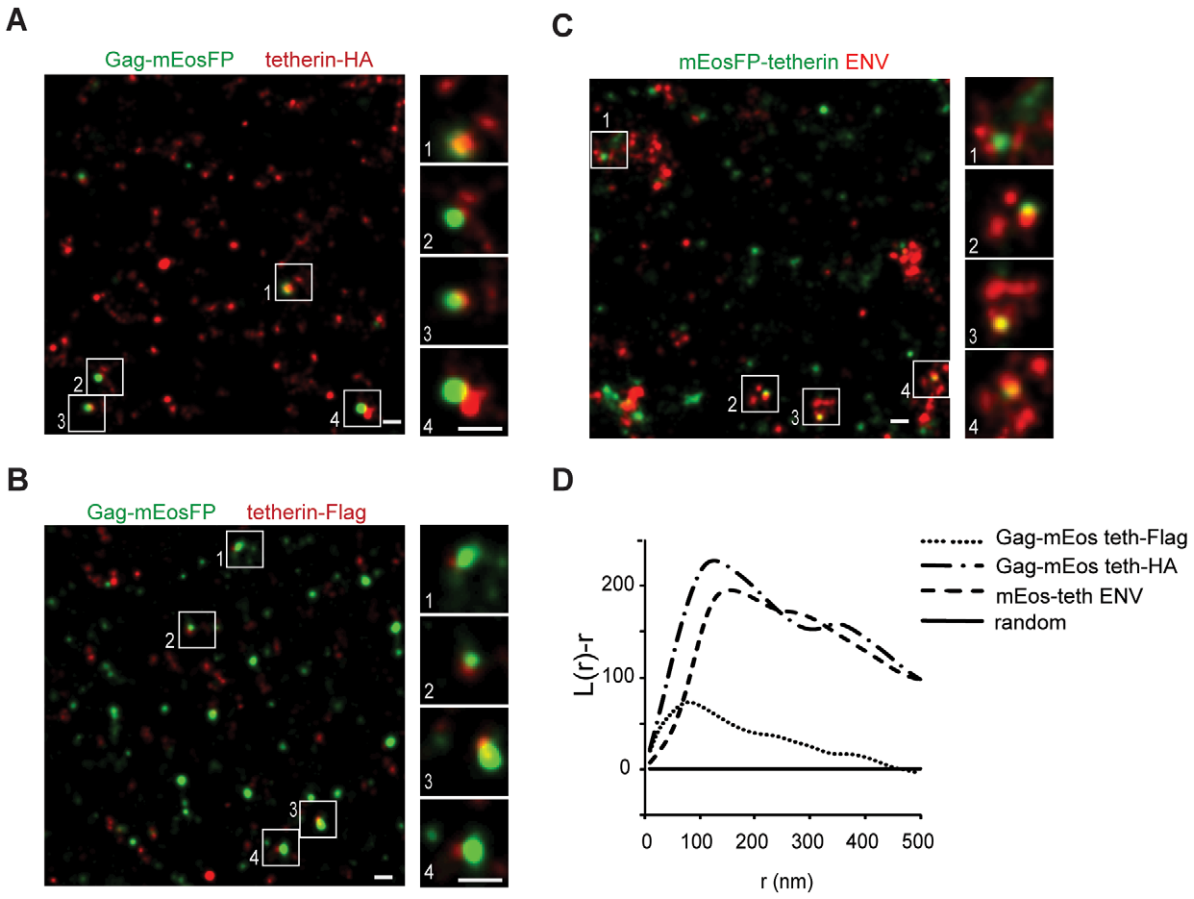

Figure 3. Single tetherin domains cocluster with HIV-1 budding sites. (A–C) Representative regions of super-resolution images of HeLa cells transfected with HIV-1 Δvpu and: (A) Gag-mEosFP and tetherin-HA; (B) Gag-mEosFP and tetherin-Flag and (C) mEosFP-tetherin. Tetherin-HA, tetherin-Flag and HIV-1 ENV were stained by indirect immunofluorescence for HA, Flag and ENV, respectively. (D) Bivariant Ripley's L analysis indicates coclustering of tetherin-HA, tetherin-Flag and mEosFP-tetherin with HIV-1 Gag-mEosFP and ENV, respectively. Images are representative of 5-10 cells from two independent transfections.
doi:10.1371/journal.ppat.1002456.g003

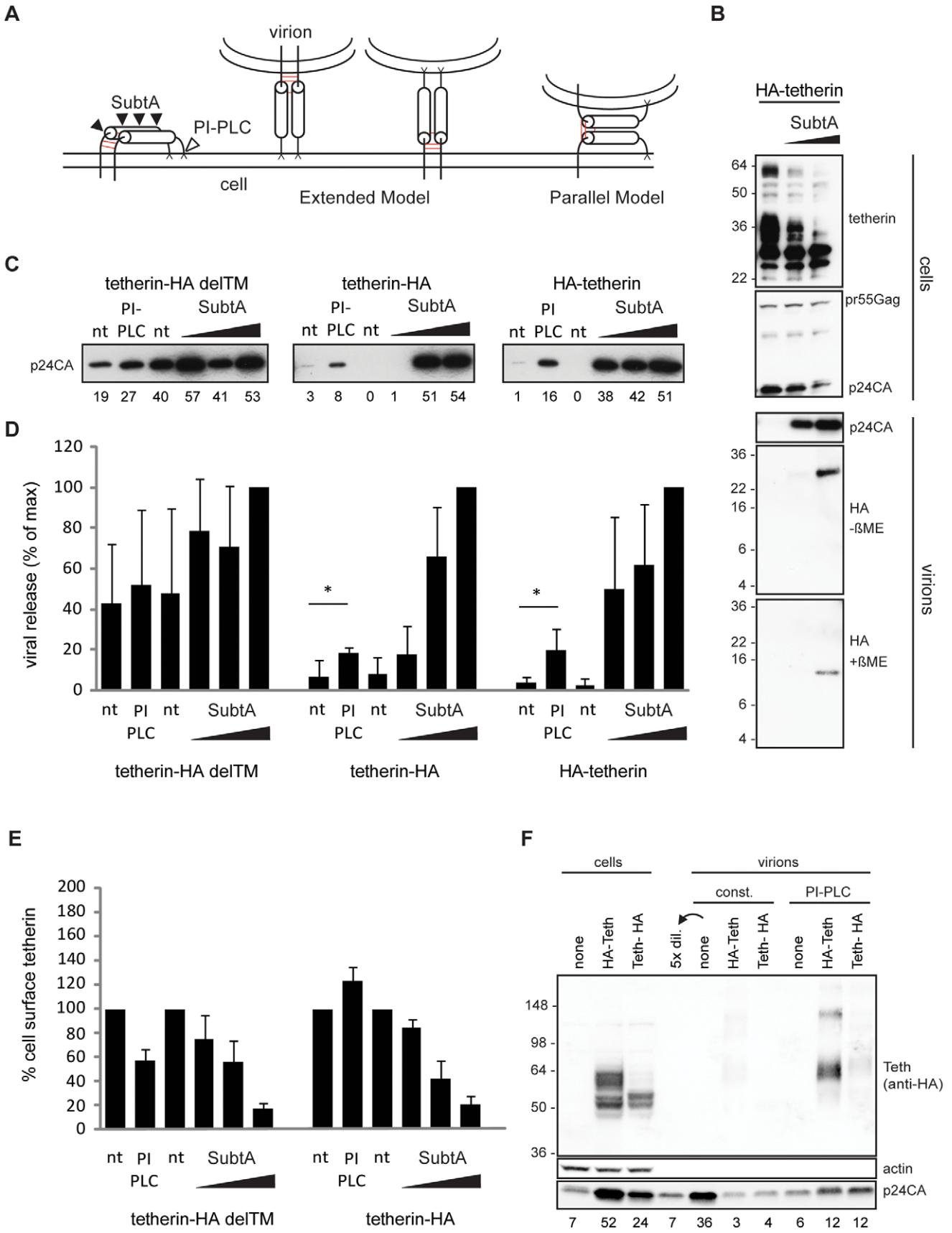
A
virion
SubtA
PI-PLC
cell
Extended Model
Parallel Model
B
HA-tetherin
SubtA
64
50
36
22
tetherin
pr55Gag
p24CA
cells
p24CA
36
22
16
6
4
HA
-ßME
HA
+ßME
virions
C
tetherin-HA delTM
tetherin-HA
HA-tetherin
PI-PLC
SubtA
nt PLC nt
PI
p24CA
19 27 40 57 41 53
3 8 0 1 51 54
1 16 0 38 42 51
D
viral release (% of max)
120
100
80
60
40
20
0
*
nt PI PLC nt SubtA
tetherin-HA delTM
tetherin-HA
HA-tetherin
E
% cell surface tetherin
200
180
160
140
120
100
80
60
40
20
0
nt PI PLC nt SubtA
tetherin-HA delTM
tetherin-HA
F
cells
virions
const.
PI-PLC
none
HA-Teth
Teth- HA
5x dil.
148
98
64
50
36
Teth
(anti-HA)
actin
p24CA
7 52 24 7 36 3 4 6 12 12

Figure 4. Tetherin restricts HIV-1 release as extended dimers. (A) Model of tetherin, enzymatic cleavage sites of subtilisin A (SubtA) and phosphatidyl-inositol-specific phospholipase C (PI-PLC) and possible orientations during restriction, disulfide bonds are represented in red. (B) Western blot analysis of subtilisin A stripped cells and virions. 293T cells transfected with HIV-1 Δvpu and HA-tetherin were treated with subtilisin A (0,5 or 50 μg/ML). Released Virions were pelleted through sucrose and analyzed under non-reducing (-βME) or reducing (+βME) SDS-PAGE/Western blot together with corresponding cell lysates (+βME). Data is representative of 2 experiments. (C) Western blot analysis (anti-p24CA) of purified virions released from non-treated (nt), PI-PLC (1 U/ML) or subtilisin A (0.2, 1 or 5 μg/ML) treated 293T cells transfected with HIV-1 Δvpu, GFP and either transmembrane-deficient tetherin-HA delTM, tetherin-HA or HA-tetherin, that contain either a C or N-termal HA-tag. Numbers below each lane indicate integrated densities in arbitrary units and are representative of 3 experiments. (D) Quantification of viral release from non-treated (nt), PI-PLC or subtilisin A treated cells 3-4 independent experiments as in B), maximal release by 5 μg/ML Subtilin A treatment was normalized to 100%. Error bars represent standard deviations and * indicates statistically significant difference with $p = 0.05$ (two-tailed paired Student's t-test). (E) Enzymatic removal of tetherin from cells in (C) was analyzed by Fluorescence-activated cell sorting (FACS). Shown are mean fluorescence intensities of anti-HA labeling in GFP-positive cells with non-treated cells set to 100%. Error bars represent standard deviations ($n = 3$). (F) Western blot analysis of PI-PLC stripped virions from 293T cells transfected with HIV-1 Δvpu and HA-tetherin or tetherin-HA. Virions that were constitutively released (const.) or released following incubation of cells with 1 U/ML PI-PLC were pelleted through sucrose. Virions and corresponding cell lysates were analyzed by Western blotting with anti-HA, anti-p24CA and anti-actin antibodies. Numbers below each lane indicate integrated densities of p24CA in arbitrary units. Sizes of molecular weight markers are shown in kilodaltons.
doi:10.1371/journal.ppat.1002456.g004

molecule numbers [37–39]. Detailed photophysical characterization of the irreversible photo-convertible mEos [40] revealed long-lived dark states of the photoactivated red form that could lead to clustering artifacts and significant overcounting [39,41]. Annibale *et al.* showed that continuous instead of pulsed photoactivation by 405 nm light and the introduction of dark times significantly reduced overcounting [41]. Following this methodology, fields of monodispersed mEosFP were used to determine appropriate imaging and analysis parameter including 561 nm excitation intensity [42], continuous 405 nm photoactivation and a dark time of 5 s. As a result, we found 1–2 reactivation events per single mEosFP molecule (25th–75th percentile range, Figure 7C and Figure S7), which may reflect the presence of a minor fraction of mEosFP multimers. Subsequently, using this optimized imaging and analysis parameters we estimated the number of mEosFP-tetherin molecules in free clusters and at HIV-1 budding sites (Figure 7A,B). At 550 assembly sites, we found 7–14 mEosFP-tetherin molecules (25th–75th percentile range, median is 10), corresponding to 4–7 tetherin dimers per budding site (Figure 7D). In contrast 400 mEosFP-tetherin clusters in the absence of HIV-1 contained 11-22 mEosFP-tetherin molecules (25th–75th Percentile range, median is 16), corresponding to 5–11 tetherin dimers (Figure 7D). The difference is significant ($p<0.001$, Student's t-test) and indicates that tetherin clusters can associate with HIV-1 budding sites. Approximately 70% of tetherin molecules within a cluster stay associated with budding virions and may participate in restricting HIV-1 release.

Discussion

We have performed biochemical and super-resolution analysis to provide further understanding of the interactions between the restriction factor tetherin and HIV-1.

First, to achieve specific and high density labeling of HIV-1 for super-resolution microscopy, we tested different monomeric PAFP in HIV-1 Gag fusions, similar to Gag-GFP that showed budding at the plasma membrane [29,30]. Gag-Dronpa, Gag-mEosFP and Dronpa-Vpr were incorporated into full HIV-1 particles, minimally affected infectivity and enabled super-resolution microscopy analysis of virions. This confirmed the expected virion diameter of 100 nm. Of note is the fact that Gag, fused to 50 kDa dimeric Eos protein, produced larger virus-like particles of 100–200 nm in initial super-resolution studies [21,28]. For multicolor super-resolution, we labeled HIV-1/cellular proteins with Dronpa, mEosFP or antibodies coupled to the photoswitchable dye Alexa Fluor 647 [24,43]. Using simultaneous detection of two fluorescent markers and high-resolution registration mapping [32] we acquired two-color super-resolution images within few minutes and with a colocalization precision of 17 nm throughout a field of view. The precise localization of antibody-labeled viral proteins within Dronpa-Vpr virions was determined by super-resolution microscopy. In accordance with PALM and electron microscopy [33] structures labeled with CA or MA antibodies had sizes of 112 nm and 117 nm, respectively and colocalized with Dronpa-Vpr. In contrast, HIV-1 integrase localized to a structure with a characteristic size of 75 nm within Dronpa-Vpr containing cores. HIV-1 ENV was predominantly found in 1–2 peripheral clusters close to Dronpa-Vpr, consistent with their localization in the viral membrane. A clustered distribution of ENV on HIV-1 virions was observed in electron tomography images and could be functionally relevant during cell attachment and fusion [35,44].

HIV-1 assembly at the plasma membrane of HeLa cells was previously visualized using diffraction-limited microscopy [29,30,45]. Super-resolution microscopy of Gag-mEosFP and antibody-stained ENV on non-permeabilized cells revealed important structural features of budding sites. Gag-mEosFP clusters of varying sizes together with clustered ENV were found in the same TIRF imaging plane close to the coverslip, indicating assembly at the plasma membrane. As previously noted, ENV was found in distinct clusters [46] that incorporated into Gag-mEosFP assembly sites. Overall, our super-resolution microscopy analysis provides a detailed picture of HIV-1 virions and their assembly sites, which was previously exclusively obtained by electron microscopy.

We applied super-resolution microscopy for the HIV-1 cellular restriction factor, tetherin. Endogenous and overexpressed tetherin were previously identified in endosomal compartments and in clusters at the plasma membrane both by fluorescence microscopy [2,3,12,15] and electron microscopy [14,15,47]. The overall clustered distribution of tetherin was not influenced by HIV-1 particle formation, however localization of tetherin at budding sites was noted in some cases [2,3,14,15], but not all [18,48]. The size of the clusters could not be determined due to the diffraction-limited resolution of conventional fluorescence microscopy or low density labeling in immuno-electron microscopy.

Using different labeling approaches for super-resolution microscopy and calibrated size measurements we found that both endogenous and overexpressed tetherins are organized in 70–90 nm clusters at the plasma membrane of HeLa cells. Annibale *et al* recently reported that dark state recovery of mEos2 can cause clustering artifacts, due to repeated localization of single molecules [41]. Since we observe similar cluster sizes for all tetherin constructs and endogenous tetherin, consistent clustering of mEosFP-tetherin using comparable imaging parameter as [41] and a significant decrease in clustering of different mutant

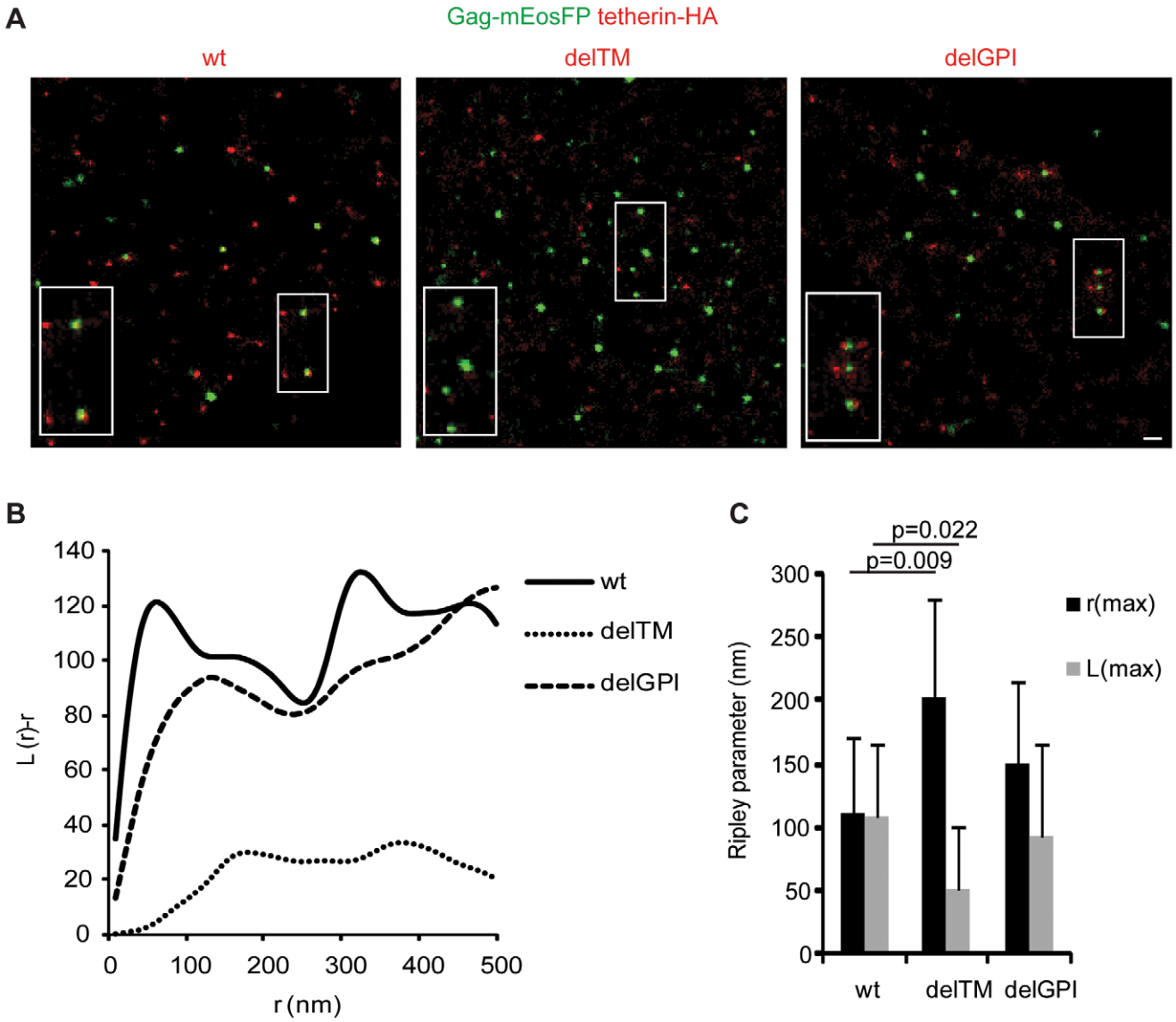

Figure 5. Association of tetherin with HIV-1 budding sites depends on its transmembrane domain. A) Representative regions of super-resolution images of HeLa cells transfected with HIV-1Δvpu, Gag-mEosFP and tetherin-HA wt, delTM or delGPI, scale bar 200 nm, B) bivariant Ripley's L analysis on fields shown in A), C) Multiple fields were analyzed by bivariant Ripley's L function and r(max) and L(max) determined, error bars represent standard deviations (9 fields from 3 cells per conditions), p values were determined by Student's t-test.
doi:10.1371/journal.ppat.1002456.g005

tetherins we report here a relevant localization of tetherin at the plasma membrane.

Notably, our increased resolution revealed that both membrane anchors of tetherin are required for clustering possibly through high order complexes between dimers [13], interaction of the cytoplasmic tail with the actin cytoskeleton [49] and lipid raft association via the GPI anchor [11].

Several models depicting the orientation of tetherin during the restriction on release of enveloped viruses have been proposed [6]. Here, we provide biochemical and microscopic evidence for HIV-1 restriction via an extended conformation of tetherin dimers. This model requires that pairs of membrane anchors incorporate into the cell membrane and the viral membrane and an extended coiled-coil domain spans the gap between both membranes (Figure 4). PI-PLC and subtilisin A treatment of 293T cells transfected with tetherin efficiently removed virions from the surface that contained dimeric tetherins. Of note, vpu-deficient HIV-1 virions were not released by PI-PLC treatment from HeLa cells, but efficient cleavage of the tetherin GPI anchor was not demonstrated [15,50]. Furthermore, slower enzymatic cleavage of the GPI anchor could occur in virion associated clusters of tetherin compared to efficient proteolytic cleavage by subtilisin A. In HeLa cells higher endocytosis rates could result in lower amounts of vpu-deficient virions bound to the cell surface compared to 293T cells [1]. Virus accumulation in biofilm-like extracellular assemblies [51] could further limit stripping efficiency by PI-PLC. Alternatively a fraction of tetherin that contains a second transmembrane domain instead a C-terminal GPI-anchor would be insensitive to PI-PLC treatment [50]. Since our results and previous reports indicate a C-terminal GPI-modification of rat and human tetherin [11,13,52] further biochemical analysis of tetherin C-terminal membrane anchor by mass spectroscopy is needed.

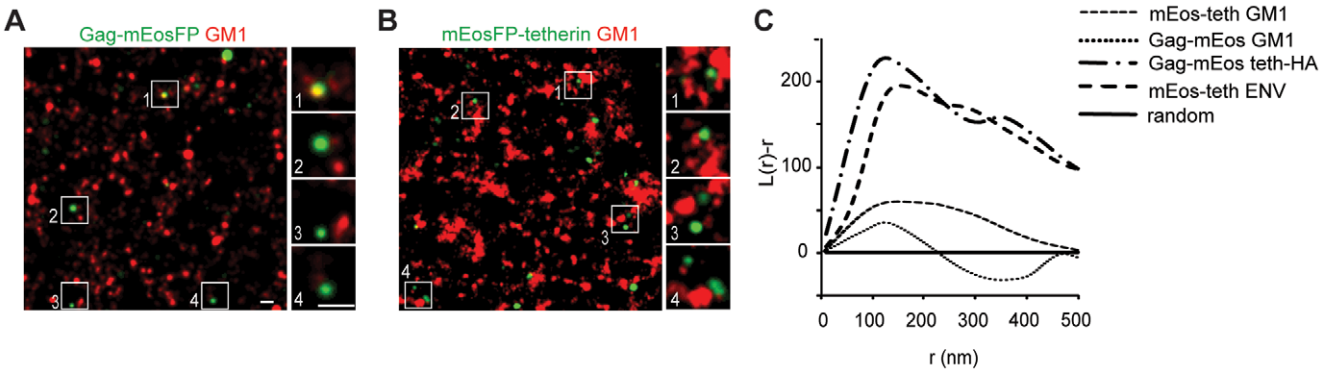

Figure 6. Tetherin domains and HIV-1 budding sites do not overlap with GM1 containing lipid rafts. (A,B) Representative regions of super-resolution images of HeLa cells transfected with HIV-1 Δvpu and Gag-mEosFP(A) or mEosFP-tetherin (B) that were fixed and stained for GM1 with Cholera toxin B Alexa Fluor 647, scale bars 200 nm (C) Bivariant Ripley's L analysis of panel A and B of this figure and Figure 3A and C Images and cocluster analysis shown is representative of multiple fields from 4–6 transfected cells from two independent transfections.
doi:10.1371/journal.ppat.1002456.g006

Of note, our biochemical analysis does not provide information on initial orientation of extended tetherin dimer at assembly sites since chains and clusters of tethered HIV-1 particles contain both of the possible orientations (Figure 4A) [13].

Therefore, we compared the incorporation of tetherin mutants lacking either the TM or GPI membrane anchor into single budding sites in HeLa cells by super-resolution microscopy. We found that the tetherin transmembrane domain stably associated with HIV-1 membranes during assembly.

Alternatively tetherin could also associate with HIV-1 budding sites via shared localization to lipid raft domains as both show some resistance to cold detergent extraction [1,11,53,54]. Both tetherin and Gag also cofractionated with the lipid raft marker caveolin [55]. Nevertheless cofractionation of proteins with raft markers does not prove their direct association or localization to similar lipid raft domains [56]. Indeed crosslinking antibodies against tetherin inhibited its antiviral effect but increased tetherin/Gag cofractionation [55].

Using super-resolution microscopy we found tetherin clusters in close association with GM1 lipid domains, but without significant overlap as previously noted for other raft proteins [57]. HIV-1 budding sites did not show significant association with GM1 lipid domains or with a tetherin mutant containing only the GPI membrane anchor. Recently HIV-1 Gag multimerization was shown to induce the coalescence of lipid raft markers and tetraspanins as visualized by antibody copatching, FRET analysis and single molecule tracking [58,59]. Both studies required copatching of raft markers (GM1, CD55 and HA–TM) and tetraspanins (CD9, CD81) to demonstrate their enrichment at HIV-1 budding sites due to the limited detection sensitivity of conventional fluorescence microscopy. Copatching could affect protein mobility and association with HIV-1 budding sites. GFP-GPI and unpatched CD55 failed to stably associate with viral assembly sites [45,59]. The later observations are consistent with our results obtained from unpatched GM-1 that was stained after fixation. Additionally the stable association of patched HA-TM and tetraspanins with viral assembly sites [58,59] is in line with our observation that clustered tetherin molecules stably associates with the viral membrane via their transmembrane domains.

Altogether the tetherin GPI modification and the association with GM1 lipid domains are not important for localization of tetherin to HIV-1 budding sites, but implicated in local concentration of tetherin (Figure 2) and maybe important for the endocytosis of retained virions. Alternatively tetherin could associate with HIV-1 assembly sites via other lipid rafts or tetraspanin-enriched domains. More efficient tetherin restriction could be obtained via late and stable incorporation into budding membranes within tetraspanin-enriched domains compared to early or transient association observed with raft markers [58,59].

At HIV-1 assembly sites, we found single tetherin clusters. mEosFP-tetherin showed a clustered plasma membrane distribution, restricted efficiently HIV-1 particle release in a Vpu-dependent manner (Figure 2A,B and Figure S6) and did not interfere with Gag assembly (Figure S6A). Therefore, the irreversible photoswitching properties of mEosFP allowed us to determine relevant mEosFP-tetherin quantities at HIV-1 assembly sites. Careful photo-physical characterization of purified mEosFP and the adjustment of imaging and analysis parameters enabled reliable single molecule counting of mEosFP.

We found 5–11 tetherin dimers in single clusters in the absence of HIV-1 and 4–7 tetherin dimers associated with HIV-1 budding sites, that represents a significant difference ($p<0.001$, Student's t-test). This indicates that about 70% of tetherin molecules within a cluster remain stably associated with budding sites possibly through incorporation of their TM domains into the viral membrane. Overall a low number of clustered tetherin dimers is sufficient to restrict the release of newly formed virions. Interestingly crosslinking antibodies against tetherin interfere with tethering function, reduce incorporation of tetherin into virions and affected the distribution of tetherin within membrane raft fractions [55]. Therefore it is possible that antibody crosslinking affects tetherin clustering, but cannot be detected by conventional diffraction limited microscopy [55]. We propose that the supramolecular organization of tetherin dimers in clusters could concentrate and position tetherin for optimal restriction and limit access to viral countermeasures. In summary, our biochemical and super-resolution analysis provided new insights into tetherin interaction with HIV-1 virions. We can propose the following mechanism for HIV-1 restriction by tetherin: Initially, tetherin locally concentrates in clusters containing 5–11 dimers and this involves both TM and GPI membrane anchors. In the absence of Vpu, tetherin N-termini associate with HIV-1 budding sites independently of GM1-enriched raft domains and become trapped during Gag-multimerization. Clusters containing 4 to 7 tetherin dimers remain associated with budding virions and can mediate restriction. Flexible coiled-coil interactions within dimers [12] are likely to enable retention of GPI anchors within the host cell membrane during budding and membrane scission. The final

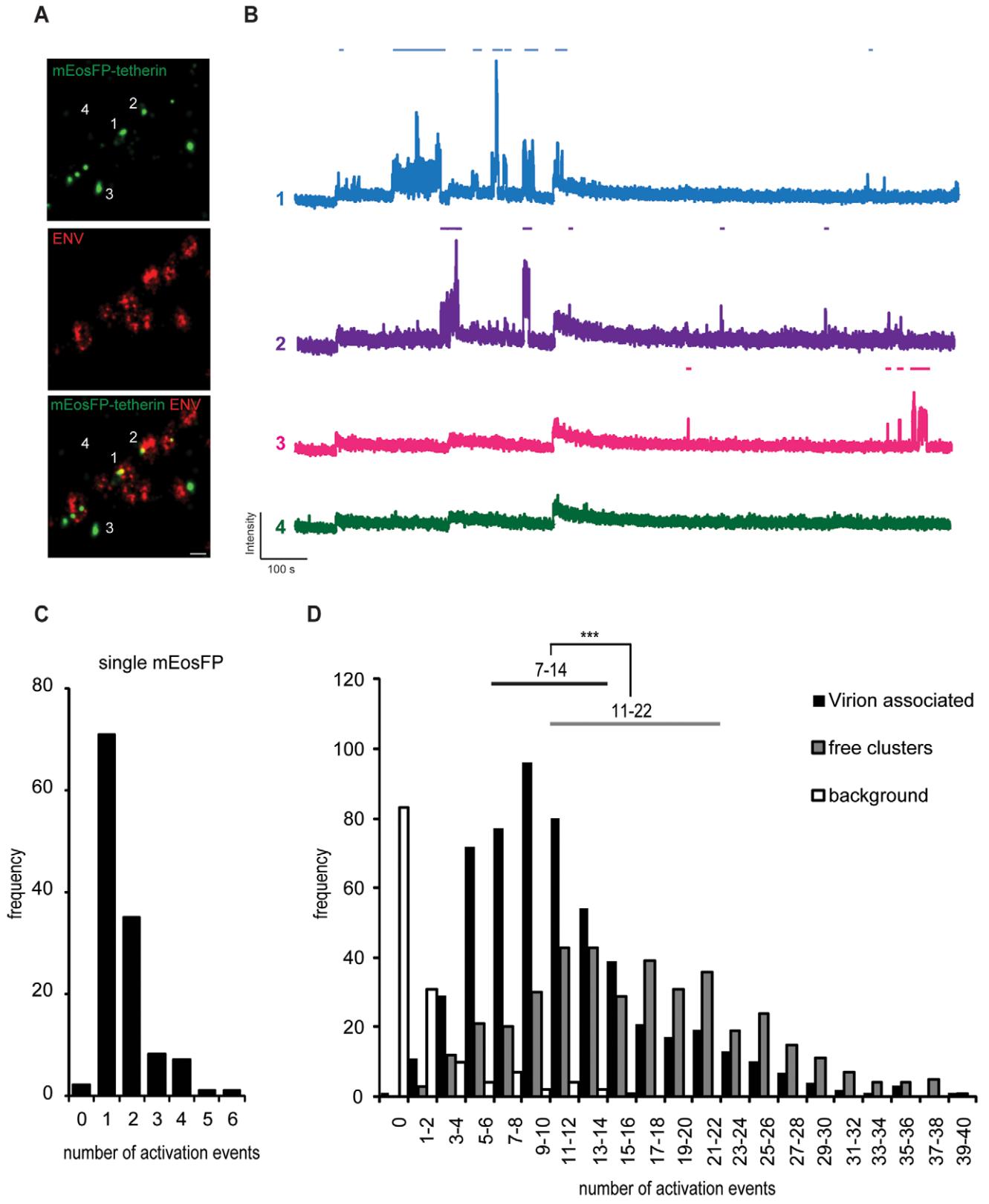

Figure 7. Single fluorescent molecule quantification of mEosFP-tetherin at HIV-1 budding sites. (A) Representative region of super-resolution images of HeLa cells transfected with HIV-1 Δvpu and mEosFP-tetherin and stained by indirect immunofluorescence for HIV-1 ENV. Acquisition was performed under alternating 561 and 644 nm excitation and continuous 405 nm photoactivation for 15 000 frames, scale bar 200 nm. (B) Intensity traces of single mEosFP-tetherin clusters as depicted in (A). Automated detection of activation events on top of each trace is depicted using a threshold of 10 standard deviations above background and a dark time of 5 s. (C) Histogram of number of activation events per single mEosFP molecules in 1% PVA (n = 125). (D) Histogram of number of activation events of mEosFP-tetherin molecules in free clusters (n = 400) or

clusters that are associated with HIV-1 budding sites (n = 550) in 5 cells. Background was selected in regions without clusters. Range indicates 25th–75th percentile. *** indicates statistically significant difference with $p<0.001$ (two-tailed paired Student's t-test).
doi:10.1371/journal.ppat.1002456.g007

predicted topology is that of extended tetherin dimers with N-termini inside newly formed virions.

Our study demonstrates that multicolor super-resolution imaging allows characterization of the interplay between viral and cellular structures with nanometer resolution. Quantitative analysis of single molecule localization in combination with biochemical analysis offers novel insights into the tetherin restriction mechanism and can be used to investigate virus-host interactions.

Materials and Methods

Cell lines

Human cell lines 293T, HeLa and HeLa-derived TZMbl were obtained through NIH AIDS Research and Reference Reagent Program and grown under standard conditions.

Plasmids and reagents

The HIV-1 expression vectors pR9 INHA (kind gift of F.D. Bushman, University of Pennsylvania) and vpu-deficient pR9 Δvpu (HIV-1 Δvpu) are based on pR9 [60]. Plasmids coding for Gag-PAFP were obtained by replacing GFP from pGag-GFP [61] with Dronpa [62], mKikGR [63], mutant mKikGR15.1 containing K141E and V160I (kind gifts from A. Miyawaki, Riken Brain Science Institute, Japan), PS-CFP2, Dendra2 [64] (both from Evrogen), mEosFP [40] (pQE32 mEosFP was a kind gift of J.Wiedenmann, University of Southampton, U.K) or PAmCherry1 [65] (kind gift of V. Verkhusha, Albert Einstein College of Medicine, NY) by standard PCR cloning. The plasmid coding for Dronpa, (pCDNA3 Dronpa) and Dronpa-Vpr was generated by standard PCR cloning. ptetherin-Flag was constructed by inserting the Flag tag after the predicted coiled-coil domain (residue 154) by PCR cloning as previously described [3]. pmEosFP-tetherin contains mEosFP separated by a spacer peptide (*ggglyksglrsra*) from tetherin N-terminus. Plasmid coding for HA-tetherin was previously described in [19]. Details for primers and cloning can be provided upon request. Plasmids coding for tetherin-HA as well as mutants delTM and delGPI [13] were a kind gift from P. Bieniasz (Aaron Diamond AIDS Research Center, NY).

Transfections, virus production and infectivity assay

293T cells were transfected using a standard calcium-phosphate-based technique. HeLa cells were transfected using Lipofectamine 2000 (Invitrogen) or Fugene HD (Roche), according to manufacturer instructions. Infectious HIV-1 particles were produced from 293T cells, filtered through a 0.45 μm filter and concentrated through 20% sucrose by centrifugation [6]. Viral titer was determined by applying limiting dilutions of filtered supernatants from producer cells on HeLa TZMbl indicator cells for 48h. Cells were fixed in 1% formaldehyde and stained for β-lactamase expression with 5-bromo-4-chloro-3-indolyl-b-D-galactoside (X-gal).

Protein and immunofluorescence analysis

Enzymatic removal of surface virions was performed by incubating transfected 293T cells 36 h post transfection with 1 U/ML PI-PLC (Invitrogen) in DMEM or 0.2–50 μg/ML subtilisin A (Sigma-Aldrich) in stripping buffer [13] for 1 h at 37°C followed by filtration and concentration through 20% sucrose. Viral pellets and cellular lysates were lysed in RIPA with protease inhibitor (Sigma) and subjected to standard SDS Page/Western blot analysis. Proteins were detected by mouse monoclonal antibodies against Dronpa (Amalgaam), HIV-1 p24CA (183-H12-5C), mature HIV-1 p17MA (4C9, kind gift from M. Marsh), HA tag (Roche), GFP (Miltenyi biotec), PCNA (Oncogene Research Products) or rabbit polyclonal antibodies against tetherin and Vpu made by K. Strebel (obtained through NIH AIDS Research and Reference Reagent Program).

Recombinant mEosFP was purified from *E. coli* BL21 DE3 transformed with pQE32 mEosFP after 5 h culture at 37°C in presence of 100 μM IPTG as described in [40]. Purified protein was desalted using PD10 columns (GE Healthcare) and protein content was determined using BCA (Thermo Scientific) against known concentrations of bovine serum albumin. For single-molecule characterization 1 nM mEosFP was prepared in 1% PVA and spin-coated on clean coverslips for 2 min at 3000 rpm.

For immunofluorescence analysis, HeLa cells or viral particles on coverslips were fixed with 3% paraformaldehyde and incubated under standard conditions with mouse monoclonal antibodies against HA-tag (Covance), Flag-tag (Sigma), HIV-1 p24CA, mature HIV-1 p17MA, mouse polyclonal antibody against tetherin (kindly provided by Chugai Pharmaceutical Co., Ltd, Kanagawa, Japan) or human monoclonal antibody against HIV-1 gp120 (2G12, obtained through NIH AIDS Research and Reference Reagent Program). Alexa Fluor 647-conjugated secondary antibodies and Alexa Fluor 647-conjugated Cholera toxin subunit B were purchased from Invitrogen. Super-resolution microscopy was performed on cells and viruses in chambered coverglass (LabTek) with freshly prepared switching buffer [24].

Super-resolution microscopy

Super-resolution microscopy was performed on an inverted microscope (Olympus IX-71) equipped with an TIRF oil objective (60x, NA 1.6, Olympus) and two simultaneously acquiring cooled Electron Multiplying-CCD (ImagEM, Hamamatsu). Dronpa was excited with 1–5 kW/cm^2 of 491 nm laser (Cobolt), mEosFP with 0.4 kW/cm^2 of 561 nm (Cobolt) and Alexa Fluor 647 with 0.3 kW/cm^2 of 644 nm (Spectra Physics) diode pumped solid state lasers. Photoactivation of photoactivatable proteins was performed with a 405 nm laser (Cube, coherent) using stroboscopic illumination [31] or continuous illumination with 0.2–1.8 W/cm^2 obtained with an optical acoustic modulator (AA Opto-Electronics). Alexa Fluor 647 was activated by 491 nm (Cobolt) or 532 nm (JP Uniphase) laser diode pumped solid state laser.

For the simultaneous measurement of Dronpa and Alexa Fluor 647, the laser lines (405, 491 and 64 nm) were combined using a 405 (zt405rdc, Chroma) and a 505 dichroic (505DCLP, Chroma) and further guided onto the sample through the same dichroic mirror (z488/633rdc, Chroma). When measuring mEosFP and Alexa Fluor 647 simultaneously, the laser lines (405, 532, 561 and 644 nm) were combined using a 405 (zt405rdc, Chroma), a 532 (z532rdc, Chroma) and a 561 dichroic (z561rdc, Chroma). The four laser lines were then guided onto the sample through the same dichroic mirror (z561/644rdc, Chroma).

Emission from TIRF illuminated sample was collected by the same objective and split by 650 long pass dichroic mirror (z650rdc, Chroma). Additional filters were used to remove excitation light and signal from other channels, namely 527/30 band pass for Dronpa (HQ527/30m, Chroma), 570 long pass and 607/67 band

pass for mEosFP (HQ570LP and HQ607/67, Chroma), 665 long pass and 700/71 band pass for Alexa Fluor 647 (HQ665LP and HQ700/71x, Chroma). The images were acquired with a final maximum field of view of ca. 41×41 μm^2 (80×80 nm^2 per pixel) with a frame rate of 10–20 Hz. In order to reduce the background and the crosstalk between the two channels, the excitation of the two fluorophores and data acquisition were synchronized using 2 mechanical shutters (NewPort). No additional stabilization of the system was required. Analysis of image sequences was performed with a homemade MATLAB routine for single molecule localization [31].

Registration mapping for two-color imaging was performed by a homemade Matlab routine. Briefly, fields of 100–400 fluorescent beads (100 nm, Tetraspek, Invitrogen) were recorded as fiducial markers in both channels. Individual bead positions were determined by Gaussian fitting for both channels, assigned automatically and used to calculate a local weighted mean mapping as described in [32] and detailed in Figure S3.

Cluster and cocluster analysis

For the determination of the cluster sizes, individual clusters were identified as discrete accumulations of 100 or more single molecule localizations within a fixed radius of 100–200 nm. The sizes were determined as 4 sigma of Gaussian function fitted to the distribution of localizations. Ripley's L function and bivariant Ripley's L function were determined from 4×4 μm^2 field of view as described [66].

Counting of mEosFP molecules

For counting the number of mEosFP molecules per cluster images were acquired using continuous illumination with 0.4 kW/cm^2 of 561 nm to excite the red form of mEosFP and 0.5–1.8 W/cm^2 405 nm laser light for photoactivation. Centers of individual clusters of mEosFP-tetherin within 100 nm from ENV staining were manually selected in two-color super-resolution images. The intensity of 9 pixels around the cluster position was measured and plotted against time for 15′000 frames. Single molecules were identified in intensity traces when intensity signals increased 10 standard deviations above background [38] using a homemade Matlab routine. Intensity increases within a dark time of 5 s were not considered to exclude blinking and recovery from long-lived dark states of activated mEosFP molecules.

Of note, the number of mEosFP-tetherin molecules represents a lower estimate since photoactivation prior to visualization, incomplete photoactivation during the experiment and missed detection of activated molecules may not be completely excluded.

Accession numbers

The human tetherin clones used in this study correspond to Swiss-Prot entries Q10589.

Supporting Information

Figure S1 Screening photoactivatable fluorescent proteins (PAFP) for HIV-1 Gag labeling and PALM. (A) Constructs used for PALM: HIV-1 Gag consisting of matrix (MA), capsid (CA), nucleocapsid (NC) and p6 was fused to different photoactivatable proteins, namely Dronpa, PS-CFP2, Dendra2, mKikGR, mEosFP and PAmCherry. Color code refers to standard emission color and gray indicates initial or photoinduced dark state. Numbers indicate wavelengths in nm used for photoactivation or excitation. (B) Western blot analysis (anti-p24CA) of cellular lysates and purified virions from 293T cells transfected with expression plasmids for HIV-1 together with indicated HIV-1 Gag-PAFP. (C) Infectivity of released virus as determined by single cycle replication assay in TZMBL cells and X-gal staining, "no PAFP" represents 100%. Error bars represent standard deviations (n≥4), (D) Labeled virions analyzed by total internal reflection fluorescence microscopy (TIRF, top row) and PALM (bottom row) for comparison purposes, scale bar 200 nm.
(TIF)

Figure S2 Setup and excitation/detection scheme used for super-resolution microscopy. Setup, excitation and detection scheme used to measure Dronpa and Alexa Fluor 647 (A) or mEosFP and Alexa Fluor 647 fluorescence (B). Specific dicroic mirrors (DM1-4) and filters (BP1-2) are described in Material and Methods. OAM: acoustic optic modulator, MS1: mechanical shutter synchronized with CCD1, MS2: mechanical shutter synchronized with CCD2.
(TIF)

Figure S3 Colocalization procedure for two-color super-resolution microscopy. 100 nm fluorescent beads were used as fiducial markers to correct differences in alignment and chromatic aberrations of detection paths (A,B). Fields of 150–500 beads were imaged simultaneously in Dronpa channel (green) and Alexa Fluor 647 channel (red) and representative part of 2×2 μm is shown. Center positions of beads were determined from Gaussian fitting and corresponding pairs of positions assigned. Localization precision for beads was found 7.6 and 6.1 nm for Dronpa (green) and Alexa Fluor 647 (red) channel, respectively (C), Pairs of center positions were used to calculate a local weighted mean transformation needed to correct images (D,E). Colocalization precision of 17±20 nm (mean ± StD, n = 1857) as measured from distances between bead positions after application of transformation (F).
(TIF)

Figure S4 Incorporation of PAFP into HIV-1 virions and size histograms. A) Immunofluorescence analysis (anti-CA, red) of HIV-1 virions containing indicated PAFP (green), scale bar 1 μm. B) Size distribution of Dronpa-Vpr, Gag-Dronpa and Gag-mEosFP in HIV-1 virions from super-resolution imaging and cluster analysis. C) Size distribution of integrase (IN), capsid (CA), matrix (MA) and Envelope (ENV) in HIV-1 virions from super-resolution imaging and cluster analysis.
(TIF)

Figure S5 Calibration of cluster size analysis. (A) Examples of simulated fields of 25 circular cluster of different sizes containing 100 random localizations, scale bar 1 μm, (B) Ripley's L analysis of simulated clusters: Note decrease of peaks and shift of maxima towards larger r at larger cluster sizes, (C) Sizes of simulated clusters were estimated using Cluster analysis or Ripley's L maxima, error bars represent StD from>6 fields. (D) Sizes of simulated clusters with varied number of localizations per cluster were estimated using cluster analysis. Error bars represent standard deviations from measurements on six fields. Note that there is no effect of number of localizations on mean cluster size
(TIF)

Figure S6 Characterisation of tetherin mutants. (A) 293T cells were transfected with HIV-1 Δvpu and either tetherin-HA, tetherin-HA delTM or tetherin-HA delGPI without or with Vpu as indicated and infectious output was determined on HeLa indicator cells. Error bars represent range of duplicate titrations. (B) Western blot analysis of cell lysates from A) was performed for pr55Gag, tetherin, Vpu, GFP as transfection control and PCNA as loading control. Note that data shown in panel A and B were obtained under identical conditions as Figure 2 B,C. (C) 293T cells

were transfected with HIV-1 Δvpu and either HA-tetherin or mEosFP-tetherin. Virions that were constitutively released (const.) or released following incubation of cells with subtilisin A (SubtA) were pelleted through sucrose. Virions and corresponding cell lysates were analyzed by quantitative Western blotting with anti-HA and anti-p24CA antibodies. Numbers below each lane indicate integrated densities of p24CA signal in arbitrary units. Sizes of molecular weight markers in B and C are shown in kilodaltons. (D) Histogram of number of mEosFP-tetherin clusters per HIV-1 budding site. Error bars represent standard deviations from quantification in 5 individual super-resolution images with a total of 550 tetherin-positive HIV-1 budding sites analyzed.
(TIF)

Figure S7 Single molecule photo-physical characterization of mEosFP. (A) SDS-PAGE and Coomassie staining of 1 or 4 μg of purified 6xHis-tagged mEosFP. Sizes of molecular weight markers are shown in kilodaltons. The predicted size of 6xHis mEosFP is 31 kDa and lower molecular weight bands represent mEosFP cleavage products associated with premature photoactivation. (B) Representative single molecule traces of mEosFP molecules in 1% PVA under 0.4 kW/cm^2 561 nm excitation and pulsed (red) or continuous (black) photoactivation (PA) by 405 nm light (0.2–0.5 kW/cm^2). Traces comprise 15 000 frames acquired with 50 ms/frame. (C) Determination of dark times (td) of the photoactivated red form of mEosFP under continuous photoactivation. Number of reactivation events per single molecule trace of (total of 15000 frames with 50 ms/frame) were determined from 25–50 traces for different t_d and 405 nm intensities. (D) Histogram of number of reactivation events per single molecule trace acquired under pulsed photoactivation (PA) or continuous PA using 405 nm light (0.5–1.8 W/cm^2) and analyzed using t_d = or 5 s. (E) Effect of excitation light on quantification of single mEosFP molecules in 1% PVA. The red form of mEosFP was detected under continuous 561 nm excitation (0.4 kW/cm^2). Continuous photoactivation by 405 nm light (1.8 W/cm^2) was switched on after 20–500 s corresponding to usual acquisition times used. Representative regions of super-resolution images are shown. Scale bar 1 μm. (F) Cluster analysis revealed similar number of detected mEosFP molecules following different exposure intervals with 561 nm excitation light as in (E). Scale bar 1 μm
(TIF)

Acknowledgments

We thank F. Leuba and A. Deres for technical assistance, F. D. Bushman, J. Wiedenmann, V. Verkhusha, A. Miyawaki and P. Bieniasz for the kind gift of reagents and Louise Kemp and Silvia Anghel for critical reading of the manuscript.

Author Contributions

Conceived and designed the experiments: ML JH VP. Performed the experiments: ML SR BM FB HU. Analyzed the data: ML SR BM FB HU. Contributed reagents/materials/analysis tools: SR BM HU. Wrote the paper: ML VP. Build set-up: SR HU ML.

References

1. Neil SJ, Eastman SW, Jouvenet N, Bieniasz PD (2006) HIV-1 Vpu promotes release and prevents endocytosis of nascent retrovirus particles from the plasma membrane. PLoS Pathog 2: e39.
2. Van Damme N, Goff D, Katsura C, Jorgenson RL, Mitchell R, et al. (2008) The interferon-induced protein BST-2 restricts HIV-1 release and is downregulated from the cell surface by the viral Vpu protein. Cell Host Microbe 3: 245–252.
3. Jouvenet N, Neil SJ, Zhadina M, Zang T, Kratovac Z, et al. (2009) Broad-spectrum inhibition of retroviral and filoviral particle release by tetherin. J Virol 83: 1837–1844.
4. Sakuma T, Noda T, Urata S, Kawaoka Y, Yasuda J (2009) Inhibition of Lassa and Marburg virus production by tetherin. J Virol 83: 2382–2385.
5. Mansouri M, Viswanathan K, Douglas JL, Hines J, Gustin J, et al. (2009) Molecular mechanism of BST2/tetherin downregulation by K5/MIR2 of Kaposi's sarcoma-associated herpesvirus. J Virol 83: 9672–9681.
6. Neil SJ, Zang T, Bieniasz PD (2008) Tetherin inhibits retrovirus release and is antagonized by HIV-1 Vpu. Nature 451: 425–430.
7. Jia B, Serra-Moreno R, Neidermyer W, Rahmberg A, Mackey J, et al. (2009) Species-specific activity of SIV Nef and HIV-1 Vpu in overcoming restriction by tetherin/BST2. PLoS Pathog 5: e1000429.
8. Sauter D, Schindler M, Specht A, Landford WN, Munch J, et al. (2009) Tetherin-driven adaptation of Vpu and Nef function and the evolution of pandemic and nonpandemic HIV-1 strains. Cell Host Microbe 6: 409–421.
9. Gupta RK, Mlcochova P, Pelchen-Matthews A, Petit SJ, Mattiuzzo G, et al. (2009) Simian immunodeficiency virus envelope glycoprotein counteracts tetherin/BST-2/CD317 by intracellular sequestration. Proc Natl Acad Sci U S A 106: 20889–20894.
10. Le Tortorec A, Neil SJ (2009) Antagonism to and intracellular sequestration of human tetherin by the human immunodeficiency virus type 2 envelope glycoprotein. J Virol 83: 11966–11978.
11. Kupzig S, Korolchuk V, Rollason R, Sugden A, Wilde A, et al. (2003) Bst-2/HM1.24 is a raft-associated apical membrane protein with an unusual topology. Traffic 4: 694–709.
12. Hinz A, Miguet N, Natrajan G, Usami Y, Yamanaka H, et al. (2010) Structural basis of HIV-1 tethering to membranes by the BST-2/tetherin ectodomain. Cell Host Microbe 7: 314–323.
13. Perez-Caballero D, Zang T, Ebrahimi A, McNatt MW, Gregory DA, et al. (2009) Tetherin inhibits HIV-1 release by directly tethering virions to cells. Cell 139: 499–511.
14. Hammonds J, Wang JJ, Yi H, Spearman P (2010) Immunoelectron microscopic evidence for Tetherin/BST2 as the physical bridge between HIV-1 virions and the plasma membrane. PLoS Pathog 6: e1000749.
15. Fitzpatrick K, Skasko M, Deerinck TJ, Crum J, Ellisman MH, et al. (2010) Direct restriction of virus release and incorporation of the interferon-induced protein BST-2 into HIV-1 particles. PLoS Pathog 6: e1000701.
16. McNatt MW, Zang T, Hatziioannou T, Bartlett M, Fofana IB, et al. (2009) Species-specific activity of HIV-1 Vpu and positive selection of tetherin transmembrane domain variants. PLoS Pathog 5: e1000300.
17. Mitchell RS, Katsura C, Skasko MA, Fitzpatrick K, Lau D, et al. (2009) Vpu antagonizes BST-2-mediated restriction of HIV-1 release via beta-TrCP and endo-lysosomal trafficking. PLoS Pathog 5: e1000450.
18. Goffinet C, Allespach I, Homann S, Tervo HM, Habermann A, et al. (2009) HIV-1 antagonism of CD317 is species specific and involves Vpu-mediated proteasomal degradation of the restriction factor. Cell Host Microbe 5: 285–297.
19. Mangeat B, Gers-Huber G, Lehmann M, Zufferey M, Luban J, et al. (2009) HIV-1 Vpu neutralizes the antiviral factor Tetherin/BST-2 by binding it and directing its beta-TrCP2-dependent degradation. PLoS Pathog 5: e1000574.
20. Bieniasz PD (2009) The cell biology of HIV-1 virion genesis. Cell Host Microbe 5: 550–558.
21. Betzig E, Patterson GH, Sougrat R, Lindwasser OW, Olenych S, et al. (2006) Imaging intracellular fluorescent proteins at nanometer resolution. Science 313: 1642–1645.
22. Hess ST, Girirajan TP, Mason MD (2006) Ultra-high resolution imaging by fluorescence photoactivation localization microscopy. Biophys J 91: 4258–4272.
23. Rust MJ, Bates M, Zhuang X (2006) Sub-diffraction-limit imaging by stochastic optical reconstruction microscopy (STORM). Nat Methods 3: 793–795.
24. Heilemann M, van de Linde S, Schuttpelz M, Kasper R, Seefeldt B, et al. (2008) Subdiffraction-resolution fluorescence imaging with conventional fluorescent probes. Angew Chem Int Ed Engl 47: 6172–6176.
25. Bates M, Huang B, Dempsey GT, Zhuang X (2007) Multicolor super-resolution imaging with photo-switchable fluorescent probes. Science 317: 1749–1753.
26. Shroff H, Galbraith CG, Galbraith JA, White H, Gillette J, et al. (2007) Dual-color superresolution imaging of genetically expressed probes within individual adhesion complexes. Proc Natl Acad Sci U S A 104: 20308–20313.
27. Huang B, Babcock H, Zhuang X (2010) Breaking the diffraction barrier: super-resolution imaging of cells. Cell 143: 1047–1058.
28. Manley S, Gillette JM, Patterson GH, Shroff H, Hess HF, et al. (2008) High-density mapping of single-molecule trajectories with photoactivated localization microscopy. Nat Methods 5: 155–157.
29. Larson DR, Johnson MC, Webb WW, Vogt VM (2005) Visualization of retrovirus budding with correlated light and electron microscopy. Proc Natl Acad Sci U S A 102: 15453–15458.
30. Jouvenet N, Bieniasz PD, Simon SM (2008) Imaging the biogenesis of individual HIV-1 virions in live cells. Nature 454: 236–240.
31. Flors C, Hotta J, Uji-i H, Dedecker P, Ando R, et al. (2007) A stroboscopic approach for fast photoactivation-localization microscopy with Dronpa mutants. J Am Chem Soc 129: 13970–13977.
32. Churchman LS, Okten Z, Rock RS, Dawson JF, Spudich JA (2005) Single molecule high-resolution colocalization of Cy3 and Cy5 attached to macromol-

ecules measures intramolecular distances through time. Proc Natl Acad Sci U S A 102: 1419–1423.
33. Briggs JA, Wilk T, Welker R, Krausslich HG, Fuller SD (2003) Structural organization of authentic, mature HIV-1 virions and cores. EMBO J 22: 1707–1715.
34. Carlson LA, de Marco A, Oberwinkler H, Habermann A, Briggs JA, et al. (2010) Cryo electron tomography of native HIV-1 budding sites. PLoS Pathog 6: e1001173.
35. Zhu P, Liu J, Bess J, Jr., Chertova E, Lifson JD, et al. (2006) Distribution and three-dimensional structure of AIDS virus envelope spikes. Nature 441: 847–852.
36. Hess ST, Gould TJ, Gudheti MV, Maas SA, Mills KD, et al. (2007) Dynamic clustered distribution of hemagglutinin resolved at 40 nm in living cell membranes discriminates between raft theories. Proc Natl Acad Sci U S A 104: 17370–17375.
37. Lillemeier BF, Mortelmaier MA, Forstner MB, Huppa JB, Groves JT, et al. (2009) TCR and Lat are expressed on separate protein islands on T cell membranes and concatenate during activation. Nat Immunol 11: 90–96.
38. Greenfield D, McEvoy AL, Shroff H, Crooks GE, Wingreen NS, et al. (2009) Self-organization of the Escherichia coli chemotaxis network imaged with super-resolution light microscopy. PLoS Biol 7: e1000137.
39. Annibale P, Vanni S, Scarselli M, Rothlisberger U, Radenovic A (2011) Quantitative photo activated localization microscopy: unraveling the effects of photoblinking. PLoS One 6: e22678.
40. Wiedenmann J, Ivanchenko S, Oswald F, Schmitt F, Rocker C, et al. (2004) EosFP, a fluorescent marker protein with UV-inducible green-to-red fluorescence conversion. Proc Natl Acad Sci U S A 101: 15905–15910.
41. Annibale P, Vanni S, Scarselli M, Rothlisberger U, Radenovic A (2011) Identification of clustering artifacts in photoactivated localization microscopy. Nat Methods 8: 527–528.
42. Jones SA, Shim SH, He J, Zhuang X (2011) Fast, three-dimensional super-resolution imaging of live cells. Nat Methods 8: 499–508.
43. Heilemann M, van de Linde S, Mukherjee A, Sauer M (2009) Super-resolution imaging with small organic fluorophores. Angew Chem Int Ed Engl 48: 6903–6908.
44. Sougrat R, Bartesaghi A, Lifson JD, Bennett AE, Bess JW, et al. (2007) Electron tomography of the contact between T cells and SIV/HIV-1: implications for viral entry. PLoS Pathog 3: e63.
45. Ivanchenko S, Godinez WJ, Lampe M, Krausslich HG, Eils R, et al. (2009) Dynamics of HIV-1 assembly and release. PLoS Pathog 5: e1000652.
46. Leung K, Kim JO, Ganesh L, Kabat J, Schwartz O, et al. (2008) HIV-1 assembly: viral glycoproteins segregate quantally to lipid rafts that associate individually with HIV-1 capsids and virions. Cell Host Microbe 3: 285–292.
47. Habermann A, Krijnse-Locker J, Oberwinkler H, Eckhardt M, Homann S, et al. (2010) CD317/tetherin is enriched in the HIV-1 envelope and downregulated from the plasma membrane upon virus infection. J Virol 84: 4646–4658.
48. Miyagi E, Andrew AJ, Kao S, Strebel K (2009) Vpu enhances HIV-1 virus release in the absence of Bst-2 cell surface down-modulation and intracellular depletion. Proc Natl Acad Sci U S A 106: 2868–2873.
49. Rollason R, Korolchuk V, Hamilton C, Jepson M, Banting G (2009) A CD317/tetherin-RICH2 complex plays a critical role in the organization of the subapical actin cytoskeleton in polarized epithelial cells. J Cell Biol 184: 721–736.
50. Andrew AJ, Kao S, Strebel K (2011) The C-terminal hydrophobic region in human BST-2/tetherin functions as a second transmembrane motif. J Biol Chem 286: 39967–39981.
51. Pais-Correia AM, Sachse M, Guadagnini S, Robbiati V, Lasserre R, et al. (2009) Biofilm-like extracellular viral assemblies mediate HTLV-1 cell-to-cell transmission at virological synapses. Nat Med 16: 83–89.
52. Masuyama N, Kuronita T, Tanaka R, Muto T, Hirota Y, et al. (2009) HM1.24 is internalized from lipid rafts by clathrin-mediated endocytosis through interaction with alpha-adaptin. J Biol Chem 284: 15927–15941.
53. Nguyen DH, Hildreth JE (2000) Evidence for budding of human immunodeficiency virus type 1 selectively from glycolipid-enriched membrane lipid rafts. J Virol 74: 3264–3272.
54. Ono A, Freed EO (2001) Plasma membrane rafts play a critical role in HIV-1 assembly and release. Proc Natl Acad Sci U S A 98: 13925–13930.
55. Miyagi E, Andrew A, Kao S, Yoshida T, Strebel K (2011) Antibody-mediated enhancement of HIV-1 and HIV-2 production from BST-2/tetherin+ cells. J Virol 85: 11981–11994.
56. Lingwood D, Simons K (2010) Lipid rafts as a membrane-organizing principle. Science 327: 46–50.
57. van Zanten TS, Gomez J, Manzo C, Cambi A, Buceta J, et al. (2010) Direct mapping of nanoscale compositional connectivity on intact cell membranes. Proc Natl Acad Sci U S A 107: 15437–15442.
58. Hogue IB, Grover JR, Soheilian F, Nagashima K, Ono A (2011) Gag Induces the Coalescence of Clustered Lipid Rafts and Tetraspanin-Enriched Microdomains at HIV-1 Assembly Sites on the Plasma Membrane. J Virol 85: 9749–9766.
59. Krementsov DN, Rassam P, Margeat E, Roy NH, Schneider-Schaulies J, et al. (2010) HIV-1 assembly differentially alters dynamics and partitioning of tetraspanins and raft components. Traffic 11: 1401–1414.
60. Naldini L, Blomer U, Gallay P, Ory D, Mulligan R, et al. (1996) In vivo gene delivery and stable transduction of nondividing cells by a lentiviral vector. Science 272: 263–267.
61. Schneider R, Campbell M, Nasioulas G, Felber BK, Pavlakis GN (1997) Inactivation of the human immunodeficiency virus type 1 inhibitory elements allows Rev-independent expression of Gag and Gag/protease and particle formation. J Virol 71: 4892–4903.
62. Ando R, Mizuno H, Miyawaki A (2004) Regulated fast nucleocytoplasmic shuttling observed by reversible protein highlighting. Science 306: 1370–1373.
63. Habuchi S, Tsutsui H, Kochaniak AB, Miyawaki A, van Oijen AM (2008) mKikGR, a monomeric photoswitchable fluorescent protein. PLoS One 3: e3944.
64. Chudakov DM, Lukyanov S, Lukyanov KA (2007) Tracking intracellular protein movements using photoswitchable fluorescent proteins PS-CFP2 and Dendra2. Nat Protoc 2: 2024–2032.
65. Subach FV, Malashkevich VN, Zencheck WD, Xiao H, Filonov GS, et al. (2009) Photoactivation mechanism of PAmCherry based on crystal structures of the protein in the dark and fluorescent states. Proc Natl Acad Sci U S A 106: 21097–21102.
66. Wendy L, Martinez ARM (2008) Computational Statistics Handbook with MATLAB. Chapman & Hall/CRC.

IκB kinase ε (IKKε) regulates the balance between type I and type II interferon responses

Sze-Ling Ng[a], Brad A. Friedman[a], Sonja Schmid[b], Jason Gertz[c], Richard M. Myers[c], Benjamin R. tenOever[b,1], and Tom Maniatis[a,d,1]

[a]Department of Molecular and Cellular Biology, Harvard University, Cambridge, MA 02138; [b]Department of Microbiology, Mount Sinai School of Medicine, New York, NY 10029; [c]HudsonAlpha Institute for Biotechnology, Huntsville, AL 35806; and [d]Department of Biochemistry and Molecular Biophysics, Columbia University, New York, NY 10032

Contributed by Tom Maniatis, November 22, 2011 (sent for review November 2, 2011)

Virus infection induces the production of type I and type II interferons (IFN-I and IFN-II), cytokines that mediate the antiviral response. IFN-I (IFN-α and IFN-β) induces the assembly of IFN-stimulated gene factor 3 (ISGF3), a multimeric transcriptional activation complex composed of STAT1, STAT2, and IFN regulatory factor 9. IFN-II (IFN-γ) induces the homodimerization of STAT1 to form the gamma-activated factor (GAF) complex. ISGF3 and GAF bind specifically to unique regulatory DNA sequences located upstream of IFN-I– and IFN-II–inducible genes, respectively, and activate the expression of distinct sets of antiviral genes. The balance between type I and type II IFN pathways plays a critical role in orchestrating the innate and adaptive immune systems. Here, we show that the phosphorylation of STAT1 by IκB kinase epsilon (IKKε) inhibits STAT1 homodimerization, and thus assembly of GAF, but does not disrupt ISGF3 formation. Therefore, virus and/or IFN-I activation of IKKε suppresses GAF-dependent transcription and promotes ISGF3-dependent transcription. In the absence of IKKε, GAF-dependent transcription is enhanced at the expense of ISGF3-mediated transcription, rendering cells less resistant to infection. We conclude that IKKε plays a critical role in regulating the balance between the IFN-I and IFN-II signaling pathways.

JAK/STAT | STAT dimerization | IFN-stimulated response element | gamma-activated sequences

Host immune defenses counteract virus infection by coordinating an intracellular innate immune response with the adaptive immune response. Systemically, the antiviral defense is generally cell-mediated, involving the recruitment and activation of dendritic cells, macrophages, neutrophils, and natural killer cells to the site of infection (1). This initial response is followed by a second wave of specific antiviral defenses involving cytotoxic T cells and antibodies generated from plasma B cells (2). The success of the adaptive immune response is intricately linked to the intracellular innate defenses initiated at the site of infection (1). The signaling required to coordinate the successful induction of the intracellular immune response to virus infection relies on the activation of interferon (IFN) genes, which encode cytokines with antiviral and immunomodulatory activity (3).

The vertebrate type I IFN (IFN-I) genes are arranged in a large gene cluster consisting of a single IFNβ gene and several tandemly arranged IFNα genes encoding distinct isotypes (4, 5). In contrast to type I IFNs, type II IFN (IFN-II) is encoded by a single IFNγ gene. Although IFN-I mediates cellular resistance to virus infection, IFN-II confers limited cellular protection through the induction of a subset of genes that are shared between the IFN-I and IFN-II transcriptomes (6, 7). Virus infection leads to the activation of IFN-I genes and the secretion of IFNα and -β, which bind to IFN receptors at the cell surface. This, in turn, leads to the transcriptional activation of a group of IFN-stimulated genes (ISGs), and these ISGs collectively establish a nonpermissive environment for virus replication (6).

The transcriptional response to IFNs is mediated by activation of the Janus kinase and signal transducer and activator of transcription (JAK/STAT) pathway (8). In this pathway, type I and type II IFNs bind to their respective receptors, leading to receptor dimerization and tyrosine phosphorylation by receptor-bound JAK kinases. These phosphotyrosines serve as docking sites for the STAT proteins via their Src homology 2 (SH2) domains (9–12). The recruitment of STAT1 and STAT2 to the receptors results in their tyrosine phosphorylation by the associated JAK kinases and their dimerization via phosphotyrosine and SH2 domain interactions in each monomer (8, 13, 14). The STAT protein dimers are then released from the receptors and translocate to the nucleus where they bind to specific regulatory DNA sequences and coordinately activate transcription of ISGs.

In the case of the IFN-I signaling pathway, both STAT1 and STAT2 are activated, leading to the formation of heterodimers that associate with the IFN regulatory factor 9 (IRF9) to form a transcription factor complex termed IFN-stimulated gene factor 3 (ISGF3) (15, 16). This complex binds to IFN-stimulated response elements (ISREs) in the promoters of ISGs, and the expression of these ISGs results in the establishment of an antiviral state (17). In contrast, IFN-II signaling results in the recruitment and tyrosine phosphorylation of two STAT1 proteins, leading to the formation of STAT1:STAT1 homodimers, a complex referred to as the gamma-activated factor (GAF) (18). GAF binds to gamma-activated sequences (GAS) found in the promoters of many genes, including a subset that is also induced by IFN-I (19). STAT1 is therefore a critical player in both IFN-I and IFN-II signaling.

We previously demonstrated that the IκB kinase ε (IKKε) phosphorylates serine 708 of STAT1 and that this phosphorylation is required for an effective antiviral response (20). However, the mechanism by which IKKε-mediated phosphorylation confers an optimal antiviral response is not known. IKKε, also known as IKKi, was originally identified on the basis of sequence similarity to the IκB kinases IKKα and IKKβ and its transcriptional induction in response to lipopolysaccharide (21–23). Following the initial discovery, IKKε and TBK1, a ubiquitously expressed homolog of IKKε, were shown to phosphorylate specific serine residues in the transcription factors IRF3 and IRF7 in response to virus infection (24–27). The phosphorylation of both transcription factors induces a conformational change and subsequent nuclear translocation where the factors bind to the IFNβ gene enhancer along with NF-κB and ATF2/cJUN to form the IFNβ enhanceosome (28, 29).

Despite the clear explanation of why the loss of IKKε renders cells more susceptible to virus infection, studies of TBK1 and IKKε knockout mice confirmed a critical role for TBK1 in the

Author contributions: S.-L.N., B.R.t., and T.M. designed research; S.-L.N. performed research; S.S. and R.M.M. contributed new reagents/analytic tools; S.-L.N., B.A.F., J.G., B.R.t., and T.M. analyzed data; and S.-L.N., B.R.t., and T.M. wrote the paper.

The authors declare no conflict of interest.

Freely available online through the PNAS open access option.

Data deposition: The sequences reported in this paper have been deposited in the European Nucleotide Archive database (accession nos. ERR033735, ERR033736, ERR033738, ERR033739, ERR033740, and ERR033741) and the Gene Expression Omnibus database, www.ncbi.nlm.nih.gov/geo (accession no. GSE33913).

[1]To whom correspondence may be addressed. E-mail: tm2472@mail.cumc.columbia.edu or benjamin.tenoever@mssm.edu.

This article contains supporting information online at www.pnas.org/lookup/suppl/doi:10.1073/pnas.1119137109/-/DCSupplemental.

induction of IFN-I, suggesting that IKKε is dispensable for this activity, except perhaps in specialized antigen-presenting cells (20, 25). The inducible nature of IKKε led to speculation that the kinase plays a redundant role to TBK1 and is responsible for activation of IRF7 late during infection; however, IKKε knockout mice failed to demonstrate defects in the induction of IRF7-depedendent IFNα isotypes (20).

We previously reported that IKKε is not required for the activation of IFN-I in response to virus infection (20). Rather, IKKε plays an important role in the IFN-I–signaling pathway. Specifically, we found that IKKε knockout mice express normal levels of IFN-I in response to influenza A virus (IAV) infection, presumably due to the presence of TBK1. However, these mice display an abnormal transcriptional response to IFN-I stimulation, leading to the loss of a critical subset of IKKε-dependent antiviral proteins and the inability to clear virus infection. Here we describe a role for IKKε in the assembly of STAT1-containing transcriptional activation complexes. Specifically, the phosophorylation of STAT1 by IKKε inhibits STAT1 homodimerization, thereby increasing the pool of STAT1 available to associate with STAT2 and IRF9 to optimally assemble the critical IFN-I transcription factor complex ISGF3.

Results

Regulation of IFN-I Signaling by IKKε Is Required for an Effective Response to IAV Infection. We infected *Ikbke*$^{+/+}$ and *Ikbke*$^{-/-}$ murine embryonic fibroblasts (MEFs) with influenza A virus (A/Puerto Rico/8/34) in the presence or absence of recombinant IFNβ (Fig. 1*A*). IAV replication in *Ikbke*$^{+/+}$ MEFs was detected 12 h post infection (hpi), as measured by nucleocapsid, hemagglutinin, and matrix protein levels, and replication was inhibited by IFNβ pretreatment. In contrast, virus replication in *Ikbke*$^{-/-}$ MEFs was detected as early as 6 hpi, revealing a significant increase in the kinetics of viral infection in the absence of IKKε. In addition, when *Ikbke*$^{-/-}$ MEFs were treated with IFNβ, there was no significant decrease in viral load, suggesting that increased IAV replication in the knockout cells is due to a defect in IFN-I signaling. These results corroborate in vivo data and support the notion that IKKε plays an essential role in coordinating the IFN-I–mediated antiviral response to IAV infection.

To examine IFN-I signaling in *Ikbke*$^{-/-}$ MEFs, we analyzed the expression of ISGs by Western blot analysis. We observed a decrease in the production of the IFN-I–dependent antiviral proteins IFIT1 (ISG56) and IFIT2 (ISG54) in *Ikbke*$^{-/-}$ MEFs compared with *Ikbke*$^{+/+}$ MEFs (Fig. 1*B*). Analysis of the kinetics of IFIT1 and IFIT2 expression reveal that these two proteins are expressed later and at reduced levels in *Ikbke*$^{-/-}$ MEFs compared with *Ikbke*$^{+/+}$ MEFs. In contrast, there was no decrease in the expression of IRF1, a protein that is primarily regulated by IFN-II and whose expression requires the GAF regulatory complex (Fig. 1*B*). However, we note that the expression of IRF1 was elevated earlier in *Ikbke*$^{-/-}$ MEFs. STAT1, another protein whose expression is predominantly GAF-regulated, was also increased in *Ikbke*$^{-/-}$ MEFs relative to wild type, an observation previously reported (20). Taken together, these data confirm that *Ikbke*$^{-/-}$ MEFs have reduced ISGF3-dependent gene expression and suggest an increase in GAF-mediated transcription.

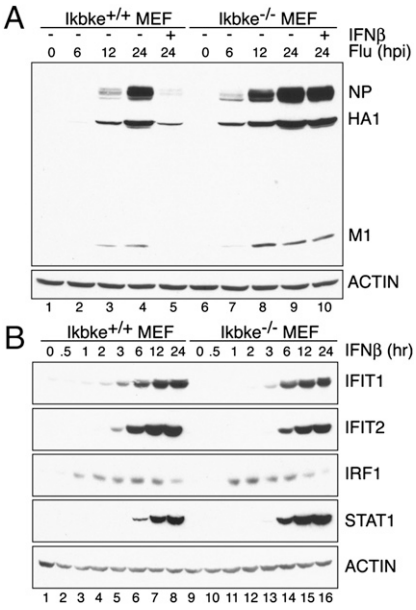

Fig. 1. IKKε knockout MEFs are susceptible to IAV infection due to an IFN-I–signaling defect. (*A*) *Ikbke*$^{+/+}$ and *Ikbke*$^{-/-}$ MEFs were infected with A/Puerto Rico/8/34 at a multiplicity of infection of 1. Cells were harvested 0, 6, 12, and 24 h post infection (hpi). Recombinant type I IFNβ was added to the media at the beginning of the 24-h infection time point. Cell extracts were analyzed by Western blot for nucleocapsid (NP), hemaggluttin (HA1), and matrix (M1) protein expression. Actin was used as a loading control. (*B*) Western blot analysis of *Ikbke*$^{+/+}$ and *Ikbke*$^{-/-}$ MEFs stimulated with IFNβ at the time points indicated. Blots depict protein levels of IFIT1, IFIT2, IRF1, and STAT1. Actin was used as a loading control. Experiments were independently repeated at least three times.

Loss of IKKε Results in Distinct IFN-I– and IFN-II–Dependent Signaling Profiles. The transcriptomes induced by IFN-I and IFN-II display considerable overlap, but are distinct (6, 7). For example, expression of Ifit1 and Ifit2 are primarily induced by IFN-I (30–32). By contrast, Irf1, Icam1, and Irf8 are primarily IFN-II–inducible genes, but lower levels can be induced by IFN-I. The overlap in the type I and II IFN transcriptomes is due in part to the activation of common factors within the IFN-I and IFN-II pathways, as well as the presence of multiple ISRE or GAS elements in many antiviral gene promoters (3, 33, 34).

To examine IFN-I– and IFN-II–induced gene transcription, we performed quantitative PCR (qPCR) analysis of *Ikbke*$^{+/+}$ and *Ikbke*$^{-/-}$ MEFs stimulated with IFNβ or IFNγ (Fig. 2). Consistent with the Western blot analysis of Fig. 1*B*, Ifit2 mRNA expression is reduced in *Ikbke*$^{-/-}$ MEFs (Fig. 2*A*). We also observed a similar decrease in levels of expression of other IFN-I–regulated genes such as Mda5 and Viperin in *Ikbke*$^{-/-}$ MEFs. In contrast, the predominantly IFN-II–stimulated genes Irf1, Irf8, and Icam1 are expressed at higher levels in *Ikbke*$^{-/-}$ MEFs compared with *Ikbke*$^{+/+}$ MEFs (Fig. 2*B*). Furthermore, qPCR analysis demonstrated that *Stat1* mRNA levels are higher in *Ikbke*$^{-/-}$ MEFs when treated with either IFNβ or IFNγ, although this increase is more pronounced with IFNγ stimulation (Fig. 2). Stat1 gene expression is inducible by both IFN-I and IFN-II, but is primarily regulated by the GAF complex (6, 7). These data

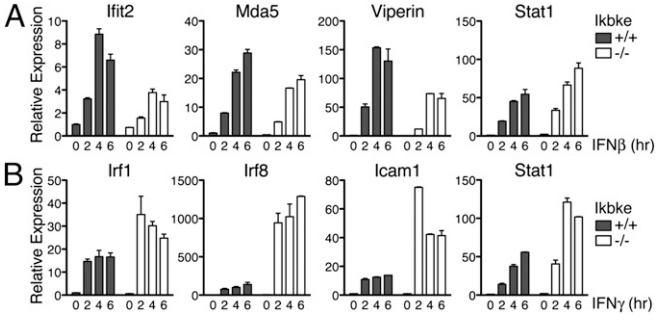

Fig. 2. Loss of IKKε impacts IFN-I– and IFN-II–mediated transcription. qPCR from RNA derived from *Ikbke*$^{+/+}$ and *Ikbke*$^{-/-}$ MEFs stimulated with IFNβ (*A*) or IFNγ (*B*) at the time points indicated. Genes analyzed include *Ifit2*, *Mda5*, *Viperin*, *Stat1*, *Irf1*, *Irf8*, and *Icam1*. All samples were normalized to *Actin* and standardized to unstimulated wild-type cells. Error bars represent SDs from triplicate measurements. Experiments were independently repeated at least three times.

clearly show that the increase in transcription of GAF-regulated genes in *Ikbke*$^{-/-}$ MEFs is inversely proportional to a decrease in expression of ISGF3-regulated genes, consistent with the hypothesis that IKKε regulates the balance in assembly and DNA binding of ISGF3 and GAF complexes.

ISGF3 Formation and Binding Decrease as GAF Formation and Binding Increase. Electrophoretic mobility shift assays were performed to examine ISGF3 and GAF complex binding in extracts from *Ikbke*$^{+/+}$ and *Ikbke*$^{-/-}$ MEFs. Cells were stimulated with IFNβ or IFNγ and analyzed for binding to either ISRE or GAS-containing DNA sequences (Fig. 3). There are at least two classes of ISREs: IKKε-dependent and IKKε-independent elements (20). As representatives of IKKε-dependent and -independent ISREs, we used elements found in the *Adar1* and *Irf7* gene promoters, respectively. The GAS sequence derives from an element in the promoter of the *Irf1* gene.

IFNβ stimulation of wild-type IKKε MEFs results in the preferential assembly and binding of ISGF3 to the ISRE probes, binding as early as 5 min post induction and maintained up to 6 h post induction (Fig. 3*A*). The kinetics of ISGF3 binding to the IKKε-independent ISRE were indistinguishable in extracts from *Ikbke*$^{+/+}$ and *Ikbke*$^{-/-}$ MEFs. In addition, competition binding studies using increasing amounts of unlabeled DNA probe showed no differences in affinity of ISGF3 to the IKKε-independent ISRE in *Ikbke*$^{+/+}$ and *Ikbke*$^{-/-}$ extracts (Fig. S1). However, consistent with the observed decrease in ISG expression, the level of ISGF3 binding to the IKKε-dependent ISRE probe was significantly reduced in *Ikbke*$^{-/-}$ MEFs compared with the *Ikbke*$^{+/+}$ MEFs (Fig. 3*A*). These observations suggest that the level of ISGF3 is lower in the *Ikbke*$^{-/-}$ extract and that the IKKε-independent ISREs have a higher affinity for ISGF3 than IKKε-dependent ISREs.

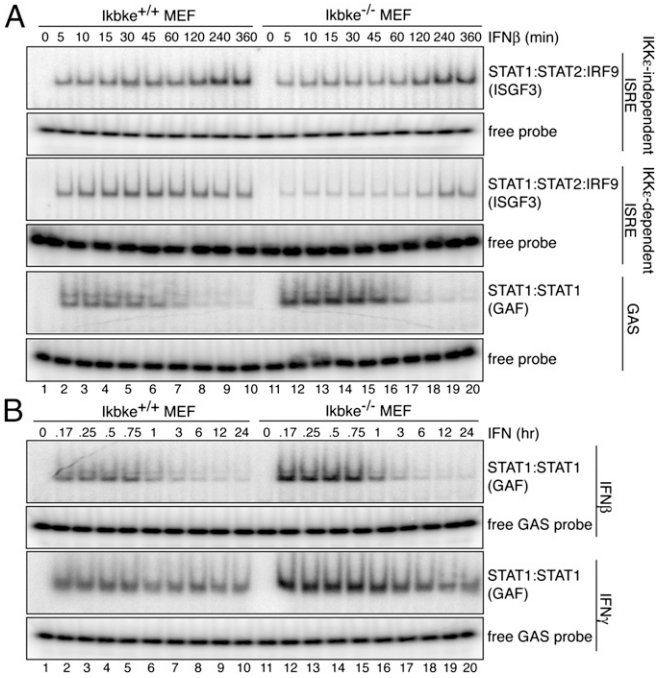

Fig. 3. ISGF3 binding decreases, whereas GAF binding increases in IKKε knockout MEFs. (*A*) EMSA with extracts derived from *Ikbke*$^{+/+}$ and *Ikbke*$^{-/-}$ MEFs stimulated with IFNβ for the time points indicated. EMSA probes include IKKε-independent ISRE, IKKε-dependent ISRE, or IRF GAS element. (*B*) EMSA with extracts derived from *Ikbke*$^{+/+}$ and *Ikbke*$^{-/-}$ MEFs stimulated with IFNβ or IFNγ for time points indicated and analyzed as in *A*. Unbound probe was used as loading control. Experiments were independently repeated at least three times.

IFN-I stimulation can also activate GAF formation and binding to a GAS probe; however, GAF binding decreases 1–2 h post stimulation (Fig. 3). In contrast to ISGF3 binding, GAF assembly and binding to the GAS element increased in *Ikbke*$^{-/-}$ MEFs relative to the wild-type control. This increase in GAF binding is observed in *Ikbke*$^{-/-}$ MEFs upon either IFNβ or IFNγ stimulation (Fig. 3*B*). Thus, an increase in GAF binding is observed in cells lacking IKKε, whereas ISGF3 binding is reduced. These differences would be expected to significantly alter the IFN-inducible transcriptome in *Ikbke*$^{-/-}$ MEFs.

The observed decrease in ISGF3 binding and concomitant increase in GAF binding may be a consequence of competition for STAT1 during formation of the ISGF3 and GAF complexes. To investigate this possibility, size-exclusion chromatography and Western blot analysis were performed to determine the relative ratio of ISGF3 and GAF in extracts from IFNβ-stimulated *Ikbke*$^{+/+}$ and *Ikbke*$^{-/-}$ MEFs (Fig. S2). Gel filtration column fractions C12 and C8 showed enriched levels of STAT1α/β, and their elution correlated with the anticipated molecular weights of ISGF3 and GAF, respectively. Higher levels of ISGF3 formation compared with GAF were observed in extracts from *Ikbke*$^{+/+}$ MEFs, whereas the ratio shifted in *Ikbke*$^{-/-}$ MEFs. We conclude that the formation and binding of ISGF3 and GAF are inversely proportional and are significantly influenced by the presence of IKKε, leading to the observed misregulation of IFN signaling.

IKKε Promotes IFN-I Signaling and Diminishes IFN-II Signaling. We have previously shown that IKKε phosphorylates the C terminus of STAT1 on serines S708, S744, and S747 (20). We therefore carried out studies to determine the effect of IKKε phosphorylation of STAT1 on the binding of ISGF3 and/or GAF complexes to the IKKε-dependent ISRE and GAS elements, respectively. We used adenovirus vectors to express either luciferase (AdV Luc) or IKKε (AdV IKKε) in E1A-expressing HeLa cells (Fig. S3). We chose these cells because E1A antagonizes IRF3-dependent activation of IFN-I gene expression (35), thereby making it possible to control IFN stimulation by exogenous introduction of IFN. The expression of AdV Luc or AdV IKKε alone did not lead to the binding of ISGF3 or GAF to an ISRE or GAS element, respectively. However, ISGF3 binding was observed upon IFN-I stimulation, and AdV IKKε did not decrease ISGF3 binding, confirming that the phosphorylation of STAT1 by IKKε does not inhibit the binding of ISGF3 to the ISRE (Fig. S3*A*). By contrast, overexpression of IKKε decreased the binding of GAF to the GAS element (Fig. S3*B*). In addition, an inverse correlation between the levels of IKKε and GAS binding was observed (Fig. S3*C*). These data provide additional evidence that IKKε reduces the level of GAF complex assembly in response to IFN stimulation.

To determine the effect of IKKε on gene expression, AdV-treated cell extracts were analyzed for expression of ISGF3-induced IFIT2 or GAS-induced IRF1 (Fig. S4). Cells treated with IFN-I or IFN-II expressed moderate levels of IFIT2 and high levels of IRF1, respectively (Fig. S4*A*). These levels were not affected by the expression of AdV Luc. In contrast, AdV IKKε treatment resulted in the induction of IFIT2 in response to IFN-II, whereas the level of IRF1 dramatically decreased following IFN-II treatment. These data provide additional evidence that IKKε plays a central role in establishing the cellular antiviral response by decreasing the expression of GAS-dependent genes and increasing the expression of ISRE-driven genes. In addition, there is an inverse correlation between the levels of IKKε and the expression of IRF1 (Fig. S4*B*), consistent with the observed decrease in GAF binding. Furthermore, as the level of IRF1 decreases in the presence of high levels of IKKε, there is a corresponding increase in the level of IFIT2. We conclude that the phosphorylation of STAT1 by IKKε shifts the cellular response toward an IFN-I–mediated transcriptome even in the presence of IFN-II.

IKKε Suppresses the Formation of Activated STAT1 Homodimers but Not STAT1:STAT2 Heterodimers. The 3D structure of the GAF complex (a STAT1 homodimer) bound to the GAS element is

known (36). This structure reveals that the STAT1 S708 residue is located within a key dimerization interface between the two STAT1 molecules. S708 engages in critical hydrogen-bonding interactions within this tightly packed interface (Fig. 4 *A* and *B*). On the basis of this structure and our previous results, we reasoned that the phosphorylation of STAT1 by IKKε may prevent STAT1:STAT1 homodimerization (in GAF formation) and thus inhibit GAS binding. However, this phosphorylation must not interfere with the interaction between STAT1 and STAT2 in the ISGF3 complex. To determine if decreased GAS binding and reduced IRF1 production results from the inability of STAT1 to homodimerize, we carried out coimmunoprecipitation experiments. However, as previously established, we found that STAT1 dimerizes in the absence of IFN, likely through an antiparallel conformation, requiring N-terminal domain interactions (37, 38). Upon IFN stimulation, STAT1 phosphorylation on Y701 results in a spatial reorientation from the antiparallel conformation to a parallel configuration, with the phosphotyrosine binding to the SH2 domain of the partner STAT1 (37, 38).

To distinguish IFN-activated parallel dimers from the unstimulated and antiparallel dimers, mutants were generated that either lacked the N-terminal 135 amino acids of STAT1 or were disrupted specifically at residues critical for preassociation (36, 37). Using these antiparallel STAT1 mutants, coimmunoprecipitation experiments were performed with cell extracts from fibroblasts exogenously expressing differentially tagged STAT1 mutants (Fig. 4*C*). Antiparallel mutant STAT1 did not associate before IFN stimulation, and dimerization was induced upon IFNγ stimulation. This dimerization was disrupted by the expression of IKKε, but not by the expression of the GFP control or the catalytically dead mutant IKKε K38A.

In contrast to STAT1 homodimerization, IKKε does not disrupt STAT1:STAT2 heterodimerization (Fig. 4*D*). It is interesting to note that IKKε expression results in a phosphorylation-dependent shift in STAT2 mobility, suggesting that IKKε may phosphorylate STAT2 in addition to STAT1. In the absence of IFN stimulation, STAT1 and STAT2 can weakly preassociate (39), and we noted that IKKε expression stabilizes this association before IFN stimulation (Fig. 4*D*, lane 2). These data suggest that phosphorylation of S708 disrupts the parallel STAT1 homodimer and facilitates a STAT1:STAT2 dimerization interface, which must differ from that of the STAT1 homodimer. The structural differences, if any, between the components in the ISGF3 complex assembled in the presence or absence of IKKε are currently unknown.

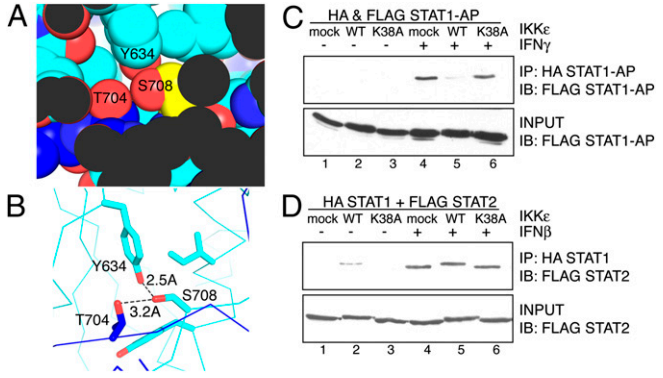

Fig. 4. IKKε phosphorylation disrupts the STAT1 homodimer, but not the STAT1:STAT2 heterodimer interface. (*A*) Space-filling diagram of the S708 (yellow) region and (*B*) hydrogen-bonding interactions of S708 in the STAT1:STAT1 homodimerization interface (light and dark blue). The diagram is adapted from the 3D structure published by Chen et al. (36) using PyMol. (*C*) 293T cells were transfected with HA STAT1 and FLAG STAT1 antiparallel (AP) mutants and GFP (mock transfected), IKKε WT, or IKKε K38A. Cells were unstimulated or stimulated with IFNγ. (*D*) 293T cells were transfected with HA STAT1 and FLAG STAT2 and GFP, IKKε WT, or IKKε K38A. Cells were unstimulated or stimulated with IFNβ. Coimmunoprecipitation experiments were performed using anti-HA matrix beads for the immunoprecipitation (IP) and immunoblotted (IB) for anti-FLAG tagged protein. Input samples were loaded as a control. Experiments were independently repeated at least three times.

Next, we performed electrophoretic mobility shift assays using purified recombinant proteins that are modified by phosphorylation and assayed for their ability to bind either the GAS or the ISRE DNA element (Fig. S5). Recombinant transcription factors were phosphorylated by the recombinant kinases JAK or IKKε. The phosphorylation of STAT1 by JAK resulted in GAF formation and binding to DNA; however, when STAT1 was both JAK- and IKKε-phosphorylated, it failed to bind to DNA. By contrast, IKKε phosphorylation of STAT1 did not disrupt ISGF3 complex formation. These data provide further evidence that IKKε phosphorylation directly regulates the STAT-mediated antiviral cellular response induced by IFN-I and IFN-II, acting as a molecular switch and integrating two independent signaling cues into a single cellular transcriptional output.

Loss of IKKε Results in Aberrant ISG Induction in Bone Marrow-Derived Macrophages. We analyzed ISG expression in bone marrow-derived macrophages (BMMs) from *Ikbke*$^{+/+}$ and *Ikbke*$^{-/-}$ mice by RNA deep sequencing (RNA-seq). Analysis of the RNA-seq data from *Ikbke*$^{+/+}$ BMMs identified a set of 538 ISGs whose levels increased at least threefold upon IFNβ or IFNγ induction. We ordered these ISGs by their beta–gamma mixture (BGM), which provides a number that reflects the fold induction in response to IFNβ and IFNγ, ranging from −1 for a purely beta response, 0 for equal response to beta and gamma, and +1 for a purely gamma response (Fig. S6*A*). The expression of individual ISGs, such as IFIT2 and IRF1, is shown, as well as the relative order of the ISGs in the BGM scale. In *Ikbke*$^{-/-}$ BMMs, IFNβ stimulation resulted in a relative decrease of previously characterized IFN-I–mediated genes and a corresponding increase in genes responsive to IFN-II.

We then examined the relationship between BGM- and IKKε-dependent gene expression (Fig. S6*B*). Although an increase in the basal level of transcription was observed for most ISGs in *Ikbke*$^{-/-}$ BMMs, genes primarily induced by IFNγ showed a significant increase in baseline expression. We also observed a positive correlation between BGM- and IKKε-dependent gene expression changes in IFNβ-stimulated cells. ISGs with negative BGM (indicating stronger IFNβ responses) were expressed at lower levels in *Ikbke*$^{-/-}$ BMMs, consistent with our observations of MEFs (20). By contrast, those ISGs with a positive BGM (indicating stronger IFNγ responses) were expressed at a higher level in *Ikbke*$^{-/-}$ BMMs. We did not observe a correlation between BGM- and IKKε-dependent changes in IFNγ-stimulated cells, but it is interesting to note that there is a general increase in IFNγ-stimulated expression of ISGs in *Ikbke*$^{-/-}$ BMMs compared with *Ikbke*$^{+/+}$ BMMs. We conclude that IKKε biases the transcriptome away from the IFN-II–signaling pathway and toward the IFN-I pathway.

Altered STAT1α Binding in the Promoters of ISGs in IKKε Knockout BMMs. To correlate transcriptional activation with STAT1-complex binding in vivo, we performed STAT1α ChIP-seq analyses on BMMs from *Ikbke*$^{+/+}$ and *Ikbke*$^{-/-}$ mice. Bone marrow from *Ikbke*$^{+/+}$ and *Ikbke*$^{-/-}$ mice were isolated, differentiated into macrophages, and either not treated or treated with IFNβ or IFNγ for 6 h before cross-linking for ChIP-seq analysis. ChIP reactions were performed with an anti-STAT1α antibody, and libraries of STAT1-bound DNA were generated for high-throughput sequencing. The ChIP-seq data confirm that IKKε-deficient BMMs have a different STAT1α-binding profile compared with wild-type BMMs, as seen in representative type I and II IFN-induced ISGs (Fig. S7). For example, the density of reads in STAT1α peaks associated with *Tlr9* and *Ifit2* is higher in *Ikbke*$^{+/+}$ BMMs compared with *Ikbke*$^{-/-}$ BMMs, indicating that STAT1α binding, in the form of ISGF3, is diminished in IKKε-deficient cells. In contrast, reads in STAT1α peaks associated

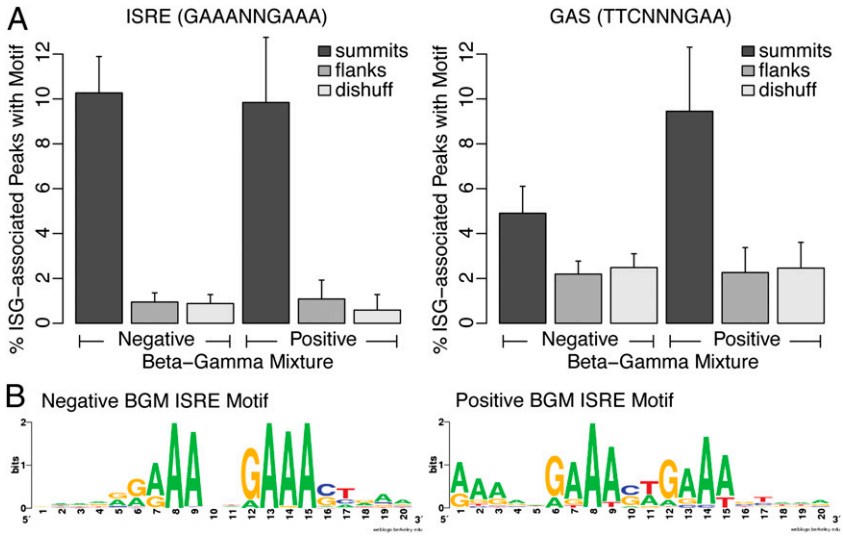

Fig. 5. Stat1α peaks near type-I and type-II ISGs are associated with different sequence motifs. (*A*) Motif frequencies in negative BGM (type-I) and positive BGM (type-II) ISG-associated peaks and control regions. For each peak associated with an ISG, a 100-bp region centered on the peak summit was extracted. As controls, each of these regions was dinucleotide shuffled (42), and also the 100 bp flanking each called peak was taken. The fraction of dinucleotide shuffled (dishuff) or flanking region (flank) controls, or real summits, containing at least one ISRE motif or GAS motif is shown. (*B*) Motifs discovered by unbiased search using BioProspector in summit regions (100 bp) associated with negative and positive BGM ISGs.

with *Nos2*, *Gbp2*, and *Irf1*, ISGs that are predominantly activated by IFN-II, do not have reduced read density in *Ikbke*$^{-/-}$ BMMs. These data confirm that STAT1α binding as the GAF complex is not inhibited in IKKε-deficient cells. In addition, *Nos2* has a higher read density in *Ikbke*$^{-/-}$ BMMs compared with *Ikbke*$^{+/+}$ BMMs. However, we did not observe a significant increase in GAF binding in *Gbp2* and *Irf1*, suggesting that STAT1α binding as the GAF complex is robust in macrophages. Thus, the primary level of regulation by IKKε appears to be in the enhancement of ISGF3 formation, thus increasing the ratio of ISGF3/GAF complex formation.

To examine the DNA sequence motifs recognized by STAT1α, we determined whether the ISRE consensus motif GAAANNGAAA or the GAS motif TTCNNNGAA was enriched in 100-bp regions surrounding the summits of STAT1α-bound peaks (Fig. 5*A*). As controls, we used random dinucleotide shuffles of the same sequences, as well as 100-bp regions flanking the called peaks. Although both motifs were enriched in summits relative to the two controls, significant differences were not observed between the percentage of ISG-associated peaks with the consensus ISRE in negative and positive BGM genes. In contrast, the GAS motif was found in a higher percentage of peaks associated with positive BGM genes than with negative BGM genes. Because the use of predefined consensus motifs may provide some limitations to the analysis, we also used an unbiased motif-finding approach to detect the motifs enriched in STAT1α peaks associated with negative and positive BGM genes (Fig. 5*B*). This method identified ISRE motifs, with the motif from the positive BGM genes containing additional purine-rich contacts. This analysis confirms the motif preference previously predicted for IKKε-independent ISREs, in which additional DNA contact points may compensate for the lack of an IKKε-modified ISGF3 complex (20, 40). Taken together, the ChIP-seq data suggest that IKKε regulates ISG transcription by promoting the assembly of STAT1 into the ISGF3 complex and suppressing STAT1 homodimerization to form GAF. We conclude that IKKε deficiency increases STAT1 incorporation into GAF, leading to the loss of crucial ISGF3-regulated antiviral gene transcription and increased susceptibility to virus infection.

Discussion

Modeling of ISGF3 based on the IRF DNA-binding domain and STAT dimers in the parallel configuration suggests that both major and minor grooves of the ISRE sequence are completely occupied by IRF9 and STAT1 on opposing strands (20). Furthermore, the ISGF3-binding specificity appears to depend on the ISRE core as well as on the surrounding sequences. We propose that the structure of the STAT1/STAT2 heterodimer within the ISGF3 complex is distinct from that of the STAT1/STAT1 homodimer. Specifically, we propose that phosphorylation of serine 708 of STAT1, located at the homodimer interface, blocks the formation of a STAT1/STAT1 homodimer but does not block the formation of the STAT1/STAT2 heterodimer within the ISGF3 complex. On the basis of the 3D structure of the STAT1 homodimer, we propose that any modification of serine, including phosphorylation, would disrupt its hydrogen-bonding interactions within this homodimerization interface. However, it appears that ISGF3 can accommodate S708 phosphorylation in the context of the trimeric complex, suggesting that, in combination with IRF9, the STAT1/STAT2 interface differs from that of the heterodimer.

Here, we demonstrate that phosphorylation of STAT1 by IKKε suppresses the formation of a parallel STAT1 dimer, thus preventing the formation of the GAF complex. This, in turn, results in the loss of GAF binding to GAS elements and a decrease in expression of GAS-dependent genes. Thus, in the context of virus infection where both IFN-I and IFN-II are produced, IKKε shifts the STAT1 pool toward the formation of ISGF3 and away from GAF. Presumably, the relative levels of phosphorylated and unphosphorylated STAT1 in cells treated with IFN-I depend on the ratio of activated IKKε to STAT1. If activated IKKε is limiting, the loss of IKKε would not affect the switch from the type I to the type II pathway. Rather, the presence of IKKε ensures that the cellular response to IFN-I and IFN-II includes the optimal production of ISGF3-dependent genes. In addition, as STAT1 forms an antiparallel configuration before JAK/STAT activation (37, 38), IKKε-mediated phosphorylation of STAT1 may be one mechanism to ensure that sufficient STAT1 is available to dimerize with other partners such as STAT2.

In addition, we show that STAT1 phosphorylation can affect the binding of ISGF3 to different types of ISREs. Specifically, we propose that the binding of ISGF3 to an IKKε-dependent minimal ISRE requires S708 phosphorylation-mediated conformational changes in ISGF3 (20). In contrast, a longer ISRE that provides additional purine-rich contact points for ISGF3 binding is IKKε independent. In the absence of IKKε, those ISGs that

are regulated by a minimal ISRE are the first to be affected. Thus, IKKε can modify IFN signaling by the regulation of STAT1 incorporation into either ISGF3 or GAF.

During the course of virus infection, IKKε expression is inducible, and IFN-I stimulation is thought to activate IKKε via p38 kinase signaling (3, 20). It is tempting to speculate that the up-regulation of IKKε serves to ensure that virus-infected cells respond to both IFN-I and IFN-II with the formation of ISGF3 to generate a cellular antiviral environment. On the basis of the evidence presented here, we propose that IKKε regulates IFN signaling by mediating STAT1 complex assembly and DNA-binding specificity. This regulation would fine-tune the ISGF3-induced gene expression profile and ensure the establishment of an effective cellular antiviral response.

Materials and Methods

Cell Culture, Viral Infections, and Reagents. Cells were cultured as described in *SI Materials and Methods*. Viral infections and reagents used are also described in *SI Materials and Methods*.

Western Blot Analysis, Coimmunoprecipitation, and Size-Exclusion Chromatography. Western blot analysis, coimmunoprecipiation, and size exclusion chromatography are described in *SI Materials and Methods*.

EMSA and Recombinant Kinase Assay. EMSA and recombinant kinase assay are described in *SI Materials and Methods*.

RNA Isolation and qPCR. RNA was isolated and qPCR was performed as described in *SI Materials and Methods*.

High-Throughput Sequencing Data Analysis. RNA-seq and ChIP-seq were performed and analyzed as described in *SI Materials and Methods*.

ACKNOWLEDGMENTS. We thank J. Ye and M. Zhao for manuscript review; D. Panne and A. García-Sastre for reagents; and E. Procko, D. Pakotiprapha, M. Lorini, and the R.M.M. laboratory for technical support. This work was supported by the National Science Foundation and Soros Fellowships (to S.-L.N.); National Institutes of Health Grant AI20642 (to T.M.); National Institute of Allergy and Infectious Diseases Grant R01AI080624 (to B.R.T.); and HudsonAlpha Institute funds (to R.M.M.).

1. Thompson AJ, Locarnini SA (2007) Toll-like receptors, RIG-I-like RNA helicases and the antiviral innate immune response. *Immunol Cell Biol* 85:435–445.
2. Baumgarth N, Choi YS, Rothaeusler K, Yang Y, Herzenberg LA (2008) B cell lineage contributions to antiviral host responses. *Curr Top Microbiol Immunol* 319:41–61.
3. Platanias LC (2005) Mechanisms of type-I- and type-II-interferon-mediated signalling. *Nat Rev Immunol* 5:375–386.
4. Hardy MP, Owczarek CM, Jermiin LS, Ejdebäck M, Hertzog PJ (2004) Characterization of the type I interferon locus and identification of novel genes. *Genomics* 84:331–345.
5. van Pesch V, Lanaya H, Renauld JC, Michiels T (2004) Characterization of the murine alpha interferon gene family. *J Virol* 78:8219–8228.
6. de Veer MJ, et al. (2001) Functional classification of interferon-stimulated genes identified using microarrays. *J Leukoc Biol* 69:912–920.
7. Der SD, Zhou A, Williams BR, Silverman RH (1998) Identification of genes differentially regulated by interferon alpha, beta, or gamma using oligonucleotide arrays. *Proc Natl Acad Sci USA* 95:15623–15628.
8. Darnell JE, Jr., Kerr IM, Stark GR (1994) Jak-STAT pathways and transcriptional activation in response to IFNs and other extracellular signaling proteins. *Science* 264: 1415–1421.
9. Greenlund AC, Farrar MA, Viviano BL, Schreiber RD (1994) Ligand-induced IFN gamma receptor tyrosine phosphorylation couples the receptor to its signal transduction system (p91). *EMBO J* 13:1591–1600.
10. Krishnan K, Singh B, Krolewski JJ (1998) Identification of amino acid residues critical for the Src-homology 2 domain-dependent docking of Stat2 to the interferon alpha receptor. *J Biol Chem* 273:19495–19501.
11. Nguyen VP, et al. (2002) Stat2 binding to the interferon-alpha receptor 2 subunit is not required for interferon-alpha signaling. *J Biol Chem* 277:9713–9721.
12. Yan H, et al. (1996) Phosphorylated interferon-alpha receptor 1 subunit (IFNaR1) acts as a docking site for the latent form of the 113 kDa STAT2 protein. *EMBO J* 15: 1064–1074.
13. Schindler C, Shuai K, Prezioso VR, Darnell JE, Jr. (1992) Interferon-dependent tyrosine phosphorylation of a latent cytoplasmic transcription factor. *Science* 257:809–813.
14. Shuai K, et al. (1994) Interferon activation of the transcription factor Stat91 involves dimerization through SH2-phosphotyrosyl peptide interactions. *Cell* 76:821–828.
15. Fu XY, Kessler DS, Veals SA, Levy DE, Darnell JE, Jr. (1990) ISGF3, the transcriptional activator induced by interferon alpha, consists of multiple interacting polypeptide chains. *Proc Natl Acad Sci USA* 87:8555–8559.
16. Levy DE, Kessler DS, Pine R, Darnell JE, Jr. (1989) Cytoplasmic activation of ISGF3, the positive regulator of interferon-alpha-stimulated transcription, reconstituted in vitro. *Genes Dev* 3:1362–1371.
17. Levy DE, Kessler DS, Pine R, Reich N, Darnell JE, Jr. (1988) Interferon-induced nuclear factors that bind a shared promoter element correlate with positive and negative transcriptional control. *Genes Dev* 2:383–393.
18. Shuai K, Schindler C, Prezioso VR, Darnell JE, Jr. (1992) Activation of transcription by IFN-gamma: Tyrosine phosphorylation of a 91-kD DNA binding protein. *Science* 258: 1808–1812.
19. Decker T, Kovarik P, Meinke A (1997) GAS elements: A few nucleotides with a major impact on cytokine-induced gene expression. *J Interferon Cytokine Res* 17:121–134.
20. Tenoever BR, et al. (2007) Multiple functions of the IKK-related kinase IKKepsilon in interferon-mediated antiviral immunity. *Science* 315:1274–1278.
21. Peters RT, Liao SM, Maniatis T (2000) IKKepsilon is part of a novel PMA-inducible IkappaB kinase complex. *Mol Cell* 5:513–522.
22. Peters RT, Maniatis T (2001) A new family of IKK-related kinases may function as I kappa B kinase kinases. *Biochim Biophys Acta* 1471:M57–M62.
23. Shimada T, et al. (1999) IKK-i, a novel lipopolysaccharide-inducible kinase that is related to IkappaB kinases. *Int Immunol* 11:1357–1362.
24. Fitzgerald KA, et al. (2003) IKKepsilon and TBK1 are essential components of the IRF3 signaling pathway. *Nat Immunol* 4:491–496.
25. Hemmi H, et al. (2004) The roles of two IkappaB kinase-related kinases in lipopolysaccharide and double stranded RNA signaling and viral infection. *J Exp Med* 199: 1641–1650.
26. Perry AK, Chow EK, Goodnough JB, Yeh WC, Cheng G (2004) Differential requirement for TANK-binding kinase-1 in type I interferon responses to toll-like receptor activation and viral infection. *J Exp Med* 199:1651–1658.
27. Sharma S, et al. (2003) Triggering the interferon antiviral response through an IKK-related pathway. *Science* 300:1148–1151.
28. Hiscott J (2007) Convergence of the NF-kappaB and IRF pathways in the regulation of the innate antiviral response. *Cytokine Growth Factor Rev* 18:483–490.
29. Maniatis T, et al. (1998) Structure and function of the interferon-beta enhanceosome. *Cold Spring Harb Symp Quant Biol* 63:609–620.
30. Berchtold S, et al. (2008) Forced IFIT-2 expression represses LPS induced TNF-alpha expression at posttranscriptional levels. *BMC Immunol* 9:75.
31. Matsumoto M, et al. (1999) Activation of the transcription factor ISGF3 by interferon-gamma. *Biol Chem* 380:699–703.
32. Zimmermann A, et al. (2005) A cytomegaloviral protein reveals a dual role for STAT2 in IFN-gamma signaling and antiviral responses. *J Exp Med* 201:1543–1553.
33. Levy DE, Darnell JE, Jr. (2002) Stats: Transcriptional control and biological impact. *Nat Rev Mol Cell Biol* 3:651–662.
34. Stark GR, Kerr IM, Williams BR, Silverman RH, Schreiber RD (1998) How cells respond to interferons. *Annu Rev Biochem* 67:227–264.
35. Juang YT, et al. (1998) Primary activation of interferon A and interferon B gene transcription by interferon regulatory factor 3. *Proc Natl Acad Sci USA* 95:9837–9842.
36. Chen X, et al. (1998) Crystal structure of a tyrosine phosphorylated STAT-1 dimer bound to DNA. *Cell* 93:827–839.
37. Mao X, et al. (2005) Structural bases of unphosphorylated STAT1 association and receptor binding. *Mol Cell* 17:761–771.
38. Mertens C, et al. (2006) Dephosphorylation of phosphotyrosine on STAT1 dimers requires extensive spatial reorientation of the monomers facilitated by the N-terminal domain. *Genes Dev* 20:3372–3381.
39. Stancato LF, David M, Carter-Su C, Larner AC, Pratt WB (1996) Preassociation of STAT1 with STAT2 and STAT3 in separate signalling complexes prior to cytokine stimulation. *J Biol Chem* 271:4134–4137.
40. Schmid S, Mordstein M, Kochs G, García-Sastre A, Tenoever BR (2010) Transcription factor redundancy ensures induction of the antiviral state. *J Biol Chem* 285: 42013–42022.
41. Becker S, Groner B, Müller CW (1998) Three-dimensional structure of the Stat3beta homodimer bound to DNA. *Nature* 394:145–151.
42. Altschul SF, Erickson BW (1985) Significance of nucleotide sequence alignments: A method for random sequence permutation that preserves dinucleotide and codon usage. *Mol Biol Evol* 2:526–538.

Supporting Information

Ng et al. 10.1073/pnas.1119137109

SI Materials and Methods

Cell Culture, Viral Infections, and Reagents. *Ikbke*$^{+/+}$ and *Ikbke*$^{-/-}$ murine embryonic fibroblasts (MEFs), HeLa E1A-expressing cells (ATCC; CRL-13002), and 293T cells were grown in Dulbecco's minimal-essential medium (DMEM) supplemented with 10% heat-inactivated FBS in a 37 °C incubator in the presence of 5% CO_2. Mouse-adapted influenza A/Puerto Rico/8/34 virus was added directly to the media at a multiplicity of infection of 1. AdV Luc and AdV IKKε (IκB kinase ε) were added directly to the media at the concentrations indicated. Recombinant interferon β (IFNβ) and IFNγ were purchased from Sigma and used at a concentration of 100 units/mL for the time points indicated. Lipofectamine 2000 and OPTI-MEM were purchased from Invitrogen and used for DNA transfection, according to the manufacturer's protocol. Expression constructs were described previously (1), and additional mutants were generated by site-directed mutagenesis using a Quikchange kit from Stratagene, according to the manufacturer's protocol.

Western Blot Analysis. Western blot analysis was performed according to standard protocols. Cell extracts were obtained following Nonidet P-40 lysis with 50 mM Tris·HCl (pH 7.4), 150 mM NaCl, 30 mM NaF, 5 mM EDTA, 10% glycerol, 40 mM β-glycerophosphate, 1% Nonidet P-40, 1 mM PMSF, 1 mM Na_3VO_4, and 5 μg/mL of leupeptin, pepstatin, and aprotinin. Protein was denatured by boiling in SDS loading buffer [50 mM Tris·HCl (pH 6.8), 2% SDS, 6% glycerol, 1% β-mercaptoethanol, and 0.004% bromophenol blue] and separated by SDS/PAGE. The gel was transferred to nitrocellulose, blocked with 5% milk, and incubated with appropriate primary antibodies. IFIT1 and IFIT2 antibodies were purchased from Thermoscientific Pierce Biotechnology. ACTIN antibody was purchased from Abcam. Influenza A antibody was a gift from Adolfo García-Sastre (Mt. Sinai School of Medicine, New York). Signal transducer and activator of transcription (STAT1) and IFN regulatory factor 1 (IRF1) antibodies were purchased from Santa Cruz Biotechnology. IKKε antibody was purchased from BioChain. Membranes were washed before and after incubation with HRP-conjugated secondary antibody. ECL reaction (Thermoscientific Pierce) was performed and protein bands visualized on film. Quantification was obtained by densitometry of the blot. Membranes were stripped using Re-Blot from Millipore and blocked again before incubation with additional primary antibodies.

Coimmunoprecipitation. 293T cells were transfected with pKH3 HA STAT1, pKH3 HA STAT1 F77/L78/F172W (referred to as HA STAT1-AP in Fig. 4*C*), pcDNA3.1 FLAG STAT1 Δ132aa (referred to as FLAG STAT1-AP in Fig. 4*C*), pCMV2 FLAG STAT2, pcDNA3 IKKε WT, pcDNA3 IKKε K38A, or pEGFP expression constructs accordingly. After overnight incubation, the cells were either unstimulated or stimulated with IFNβ or IFNγ, and protein was harvested by cell lysis with Nonidet P-40 lysis buffer. Anti-HA affinity matrix from Roche was used for the pulldown at 4 °C. Protein was eluted from the matrix by boiling in SDS loading buffer and then separated by SDS/PAGE. An aliquot of total protein (input) was also run. The gel was transferred to nitrocellulose, blocked with 5% milk, and incubated with FLAG M2 primary antibody from Sigma to detect the coimmunoprecipitated protein. Membranes were washed before and after incubation with HRP-conjugated secondary antibody. ECL reaction (Thermoscientific Pierce) was performed and protein bands visualized on film.

Size-Exclusion Chromatography. Size-exclusion chromatography was performed with cell extracts obtained following Nonidet P-40 lysis. Extracts were loaded on a Superdex200 16/60 column from GE Healthcare and eluted with 50 mM Tris·HCl (pH 7.4), 150 mM NaCl, 30 mM NaF, 5 mM EDTA, 10% glycerol, 40 mM β-glycerophosphate, and 1% Nonidet P-40. Standards (aprotinin, ribonuclease A, carbonic anhydrase, ovalbumin, conalbumin, and aldolase) were run on the column to determine elution time. Fractions were analyzed by standard Western blot analysis.

Electrophoretic Mobility Shift Assay. Protein–DNA-binding assays were performed with cell extracts obtained following Nonidet P-40 lysis. T4 PNK from New England BioLabs was used to end-label EMSA probes with γ32ATP. Protein extracts were normalized in 10 mM Hepes (pH 7.9), 2% glycerol, 40 mM KCl, 1 mM EDTA (pH 8.0), 0.2 mM $MgCl_2$, and 1 mM DTT in a total volume of 15 μL. Nonspecific binding was reduced with the addition of 1 μg of poly(dI:dC) from Amersham. Unlabeled cold competitor probe was then added, if required. The reaction was incubated on ice for 30 min before incubation with 100,000 counts per unit (CPU) of labeled double-stranded probe for 20 min at room temperature (25 °C). Samples were resolved on a 7% native gel composed of 49:1 acrylamide:bis-acrylamide in a 0.5× Tris/borate/EDTA (TBE)-based buffer. Gels were dried and exposed by autoradiogram and/or PhosphoImager. Probe sequences were the following: Adar1 IFN-stimulated response element (ISRE) (5′-CGGGGAAGCCTTTTCAAGGAAACGAAAGTGAACTC-3′), Irf7 ISRE (5′-GAAAATGAAACCTAAACAGTCTAA-3′), and Irf1 gamma-activated sequences (GAS) (5′-CATTTCGGGGAAATCGATC-3′).

Recombinant Kinase Assay. Recombinant Janus kinase (JAK) was purchased from Invitrogen. Recombinant FLAG-tagged IKKε kinase was expressed and purified from baculovirus-infected Sf21 insect cells. Recombinant histidine (HIS)-tagged STAT1, STAT2, and IRF9 was expressed and purified from BL21 bacteria. The expression constructs were a gift from Daniel Panne (European Molecular Biology Laboratory, Grenoble, France). The affinity-purified protein was concentrated and further purified by size-exclusion chromatography with 20 mM Hepes (pH 7.5), 150 mM NaCl, 1 mM DTT, and 1 mM benzamidine. Recombinant substrate and either water or recombinant IKKε kinase was incubated in the presence of 50 mM Tris·HCl (pH 7.5), 4 mM $MgCl_2$, 4 mM $MnCl_2$, and 1 mM ATP for 30 min at 30 °C. Next, either water or recombinant JAK kinase was added and incubated for another 30 min at 30 °C. The phosphorylated transcription factors were then analyzed for their ability to bind DNA in an EMSA reaction.

RNA Isolation and Quantitative PCR. RNA was extracted with TRIzol from Invitrogen and further purified using RNeasy columns from Qiagen, according to the manufacturer's instructions. Five micrograms of RNA was reverse-transcribed with SuperScript III from Invitrogen for 1 h at 50 °C using random 10mer oligo primers and resuspended in a total volume of 200 μL. Five microliters was used as template in quantitative PCR reactions using the Brilliant SYBR Green QPCR Core Reagent Kit from Stratagene, according to the manufacturer's instructions. Primers (5′–3′) used include the following: IFIT2—5′-CCTGAGCCTTTGAGAACTGG-3′ and 5′-CAATGCTTAGGGGAAGCTGA-3′; MDA5—5′-TGCAGGTGCAAAGTATCCTG-3′ and 5′-CTGGCCACACTTGCAGATAA-3′; VIPERIN—5′-CTTCAACGTGGACGAAGACA-3′ and 5′-ATTCAGGCACCAAACAGG-

AC-3′; STAT1—5′-GACCACCTCTCTTCCTGTCG-3′ and 5′-TGCCAACTCAACACCTCTGA-3′; IRF1—5′-CCTGGGTCAGGACTTGGATA-3′ and 5′-TTCGGCTATCTTCCCTTCCT-3′; IRF8—5′-AGCTGGGTTACATGCTCCAC-3′ and 5′-TAGCACTCCTTGAGGCAGGT-3′; ICAM1—5′-TTCACACTGAATGCCAGCTC-3′ and 5′-CTTCCGTCTGCAGGTCATCT-3′; and ACTIN—5′-CCTCTATGCCAACACAGTGC-3′ and 5′-ACATCTGCTGGAAGGTGGAC-3′.

RNA-seq Analysis. Bone marrow from *Ikbke*$^{+/+}$ and *Ikbke*$^{-/-}$ mice was isolated, differentiated into macrophages with macrophage colony-stimulating factor (M-CSF), and either not treated or treated with IFNβ or IFNγ for 6 h before harvesting for RNA isolation. Paired-end RNA-seq libraries were prepared by standard Illumina protocols and 36 bases were sequenced from both ends using the Illumina platform. The ExpressionPlot platform (http://expressionplot.com/) was used to analyze gene expression (2). Briefly, reads were aligned to the mouse genome (mm9) using Bowtie (3), and then nonaligning reads were aligned to a reads per kilobase gene model per million reads sequenced (RPKM) splice junction database. Only unique best alignments were used for further analysis. gene levels were calculated by counting genomic and splice alignments for each Unversity of California at Santa Cruz knownGene cluster (as defined in the knownIsoforms table, http://genome.ucsc.edu/). RPKM normalizes for the length of each gene (here using total exonic bases from any isoform) and for the effective total number of reads in each sample. Errors shown in bar plots were calculated by Poisson approximation $\sqrt{(n+1)}$. *P* values for pairwise changes were calculated using a binomial test, using the Minimize Significant Changes (MSC)-calculated effective total read numbers. Binary Sequence Alignment/Map (BAM) files for RNA-Seq available at the European Nucleotide Archive website (http://www.ebi.ac.uk/ena) with the following run IDs: ERR033735 (WT untreated), ERR033736 (WT IFNβ), ERR033738 (WT IFNγ), ERR033739 (KO untreated), ERR033740 (KO IFNβ), and ERR033741 (KO IFNγ).

Beta–Gamma Mixture. Beta–gamma mixture (BGM) provides a number for each IFN-stimulated gene factor (ISG) that indicates its relative induction by IFNβ and IFNγ. A BGM of −1 indicates that the ISG is stimulated only by IFNβ, 0 indicates equally by both IFNβ and IFNγ, and 1 indicates only by IFNγ. Conceptually, each gene's log-fold change (IFN/control) is thought of as a point (x, y) where x is the IFNβ-induced log change and y is the IFNγ-induced log change. Negative coordinates are converted to 0 (at least one must be positive because we consider only ISGs). The angle of the ray from the origin to the point is then rescaled from 0 to 90 ° to the range −1 to 1. The following R code calculates this value. It begins with lfc, a matrix with rows corresponding to ISGs and columns named "b" and "g" containing the log-fold change upon IFNβ and IFNγ stimulation:

```
ind <- ifelse(lfc > 0, lfc, 0)
tan.theta <- ind[,"g"]/ind[,"b"]
theta <- atan(tan.theta)
bgm <- theta*4/pi – 1.
```

The first line converts negative log-fold changes (cases where the gene level goes down slightly upon IFN treatment) to 0. This has the effect of projecting each point into the first quadrant. The second line calculates the tangent of the angles to each of the (x, y) points. The third line calculates the angles using the inverse tangent. Finally, the last line rescales the $[0, \pi/2]$ interval to $[-1, 1]$.

ChIP-seq Analysis. Bone marrow from *Ikbke*$^{+/+}$ and *Ikbke*$^{-/-}$ mice was isolated, differentiated into macrophages with M-CSF, and either not treated or treated with IFNβ or IFNγ for 6 h before cross-linking for chromatin isolation. ChIP reactions were performed with anti-STAT1α antibody from Santa Cruz, and libraries were generated by standard Illumina protocols. ChIP-seq and input libraries were sequenced 36 bases from a single end using Illumina platform, and reads were aligned to the genome using Bowtie. STAT1α peaks were called using MACS (4) for each IP/Input pair, and overlapping peaks from different conditions were merged to form a unified set of 47,093 potential binding sites. Binding RPKMs were then calculated by normalizing for both total number of aligning reads and peak width for each of the merged peaks. Peaks were then assigned to gene clusters by identifying the closest splice site or transcript start or end of any "canonical" isoform (knownCanonical table from Unversity of California at Santa Cruz). Motif frequencies were determined by looking for the presence of an ISRE (TTTCNNTTTC) or GAS (TTCNNNGAA) site within a 100-bp region centered on the peak summit (actually 101 bases: 50 on both sides of the summit). As controls, each of these regions was dinucleotide shuffled (5), and also the 100-bp regions flanking each called peak on both sides were taken. The fraction of dinucleotide shuffled (dishuff) or flanking region (flank) controls, or real summits, containing at least one ISRE or GAS motif was determined. Error bars are given 95% binomial confidence intervals. Finally, unbiased motif discovery was performed on the summit regions using BioProspector (6). ChIP-seq data is available in NCBI's Gene Expression Omnibus database, http://www.ncbi.nlm.nih.gov/geo (accession no. GSE33913).

1. Tenoever BR, et al. (2007) Multiple functions of the IKK-related kinase IKKepsilon in interferon-mediated antiviral immunity. *Science* 315:1274–1278.
2. Friedman BA, Maniatis T (2011) ExpressionPlot: A web-based framework for analysis of RNA-Seq and microarray gene expression data. *Genome Biol* 12:R69.
3. Langmead B, Trapnell C, Pop M, Salzberg SL (2009) Ultrafast and memory-efficient alignment of short DNA sequences to the human genome. *Genome Biol* 10:R25.
4. Zhang Y, et al. (2008) Model-based analysis of ChIP-Seq (MACS). *Genome Biol* 9:R137.
5. Altschul SF, Erickson BW (1985) Significance of nucleotide sequence alignments: A method for random sequence permutation that preserves dinucleotide and codon usage. *Mol Biol Evol* 2:526–538.
6. Liu X, Brutlag DL, Liu JS (2001) BioProspector: Discovering conserved DNA motifs in upstream regulatory regions of co-expressed genes. *Pac Symp Biocomput* 127–138.

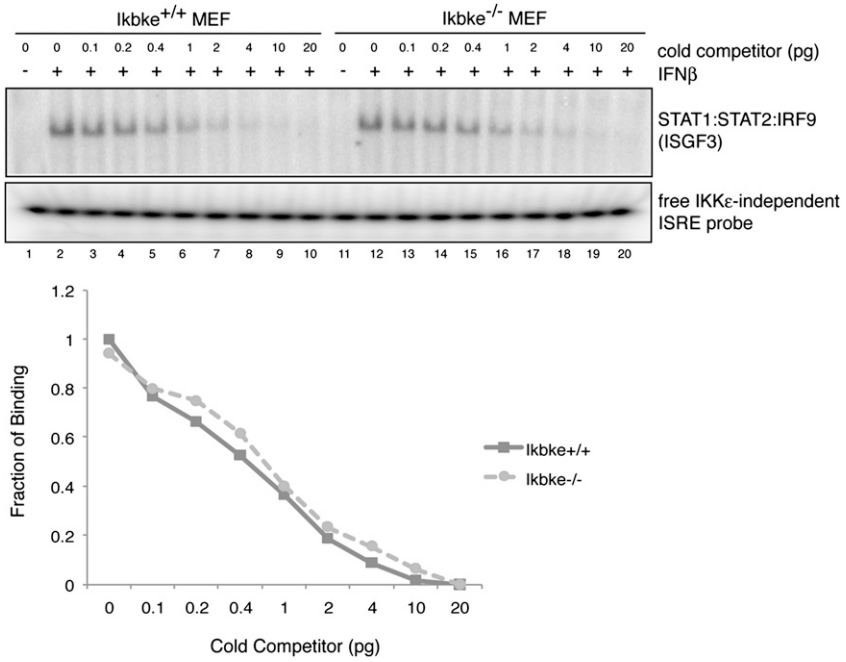

Fig. S1. Affinity of ISGF3 binding to IKKε-independent probe is unchanged in IKKε knockout MEFs. *Ikbke*$^{+/+}$ and *Ikbke*$^{-/-}$ MEFs were stimulated with IFNβ before harvesting. Cell extracts were analyzed by EMSA for binding to an IKKε-independent ISRE probe. Increasing amounts of cold probe were added as a competitor to radioactive P^{32}-labeled ISRE binding. Unbound probe was used as loading control.

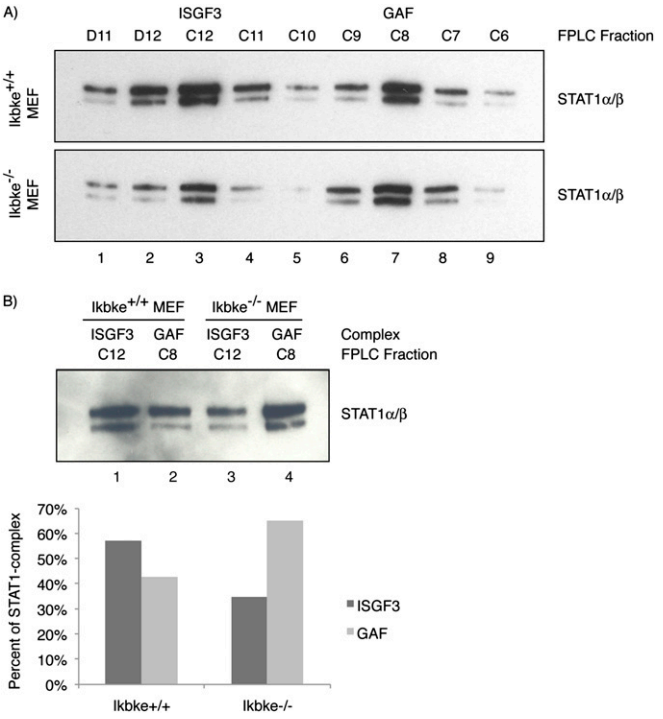

Fig. S2. Relative levels of STAT1-containing complexes differ between wild-type and IKKε knockout MEFs. (*A*) *Ikbke*$^{+/+}$ and *Ikbke*$^{-/-}$ MEFs were stimulated with IFNβ before harvesting. Cell extracts were analyzed by gel filtration, and Western blot analysis was performed for STAT1α/β. The elution time of STAT1-containing fractions was compared with standards of known molecular weight. (*B*) The percentage of each STAT1-containing complex was determined for each sample by densitometry of the Western blot.

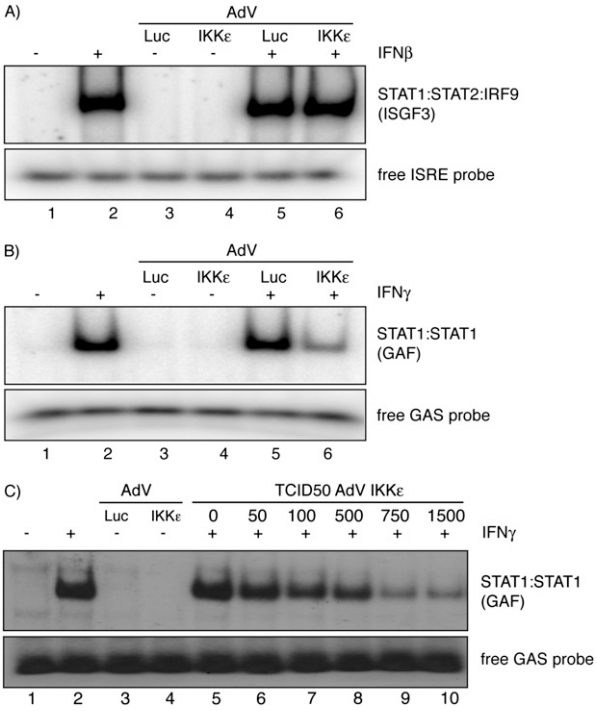

Fig. S3. Elevated levels of IKKε decrease GAF, but not ISGF3, binding. HeLa E1A-expressing cells were not treated or treated with AdV Luc or AdV IKKε to overexpress the kinase. (*A*) Cells were mock-treated or stimulated with IFNβ for 6 h before harvesting protein. ISGF3 complex binding to an ISRE probe was analyzed using the EMSA. (*B*) HeLa E1A cells were mock-treated or stimulated with IFNγ for 6 h before harvesting protein. GAF complex binding to a GAS probe was determined by EMSA. (*C*) Increasing amounts of AdV IKKε were used, and binding of GAF complex to GAS probe was determined by EMSA. Unbound probe was used as loading control. TCID50, tissue culture infectious dose 50.

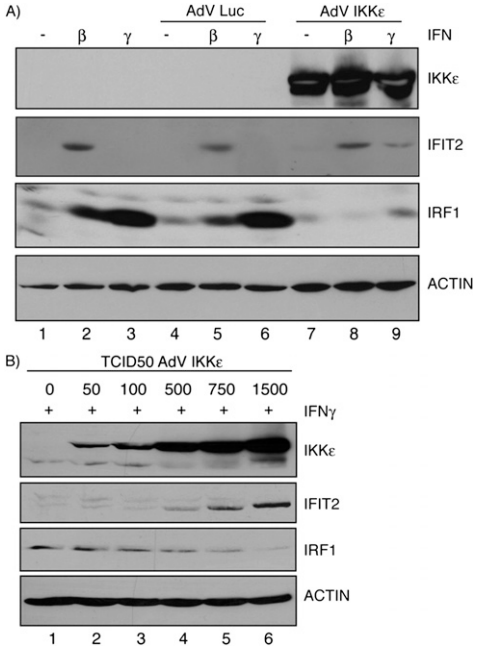

Fig. S4. IKKε overexpression decreases IRF1 expression and increases IFIT2 expression. HeLa E1A-expressing cells were not treated or treated with AdV Luc or AdV IKKε. (*A*) The cells were not stimulated or stimulated with IFNβ or IFNγ for 6 h before harvesting for protein. Expression of IKKε, IFIT2, and IRF1 was analyzed by Western blot analysis. Actin was used as a loading control. (*B*) Increasing amounts of AdV IKKε were used, and expression of IKKε, IFIT2, and IRF1 were analyzed by Western blot analysis. Actin was used as a loading control. TCID50, tissue culture infectious dose 50.

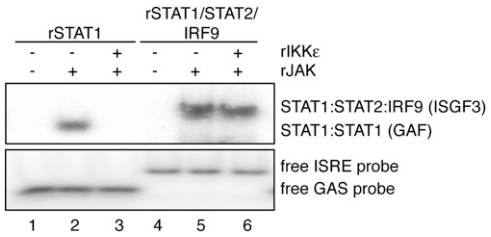

Fig. S5. IKKε phosphorylation disrupts GAF binding to DNA but not ISGF3 binding. Recombinant STAT1, STAT2, and IRF9 were phosphorylated in vitro. The substrate was incubated with recombinant IKKε kinase for 30 min at 30 °C, followed by incubation with recombinant JAK kinase for another 30 min at 30 °C. Recombinant STAT1 was analyzed for binding to GAS probe, and recombinant STAT1/STAT2/IRF9 was analyzed for binding to ISRE probe. Unbound probe was used as a loading control.

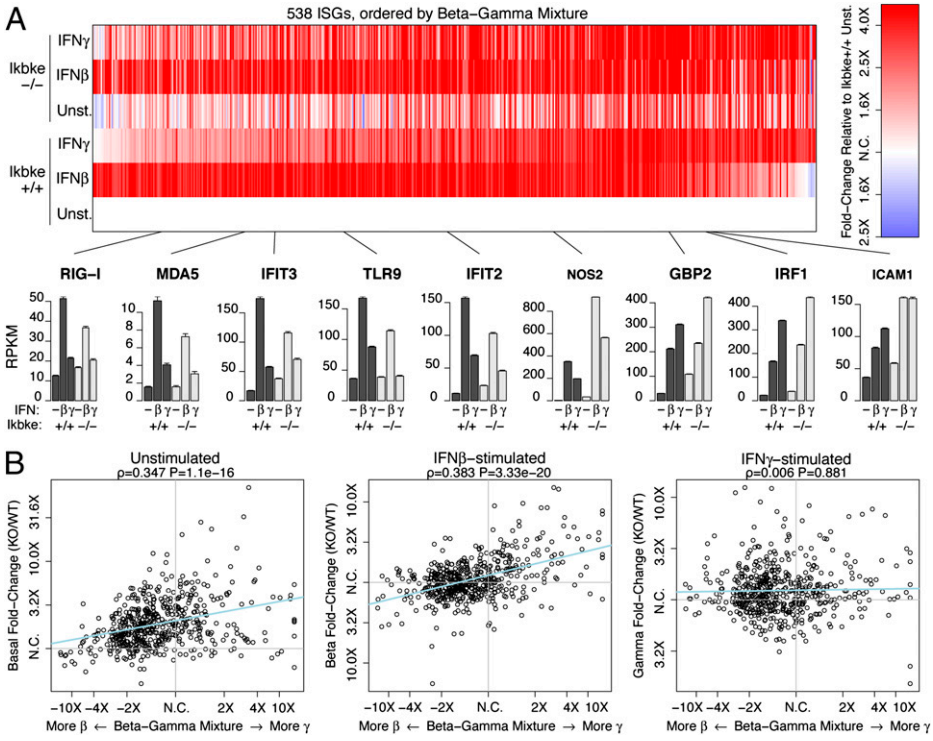

Fig. S6. IKKε biases the IFN-I–mediated transciptome over IFN-II signaling in BMMs. RNA-seq was performed on *Ikbke*$^{+/+}$ and *Ikbke*$^{-/-}$ BMMs in the presence or absence of IFNβ or IFNγ for 6 h. The 538 genes that were up-regulated at least threefold by IFNβ or IFNγ in *Ikbke*$^{+/+}$ BMMs relative to unstimulated cells were designated as ISGs. (*A*) (*Upper*) Heat map showing gene levels of 538 ISGs in all six experiments, normalized to unstimulated *Ikbke*$^{+/+}$ BMMs. Genes are ordered by their relative induction by IFNβ (*Left*) or IFNγ (*Right*). (*Lower*) Gene levels in reads per kilobase gene model per million reads sequenced (RPKM) for nine representative genes. (*B*) Scattergrams comparing relative IFNβ/IFNγ induction in *Ikbke*$^{+/+}$ BMMs for each ISG on the *x* axis and IKKε-dependent changes in gene expression on the *y* axis.

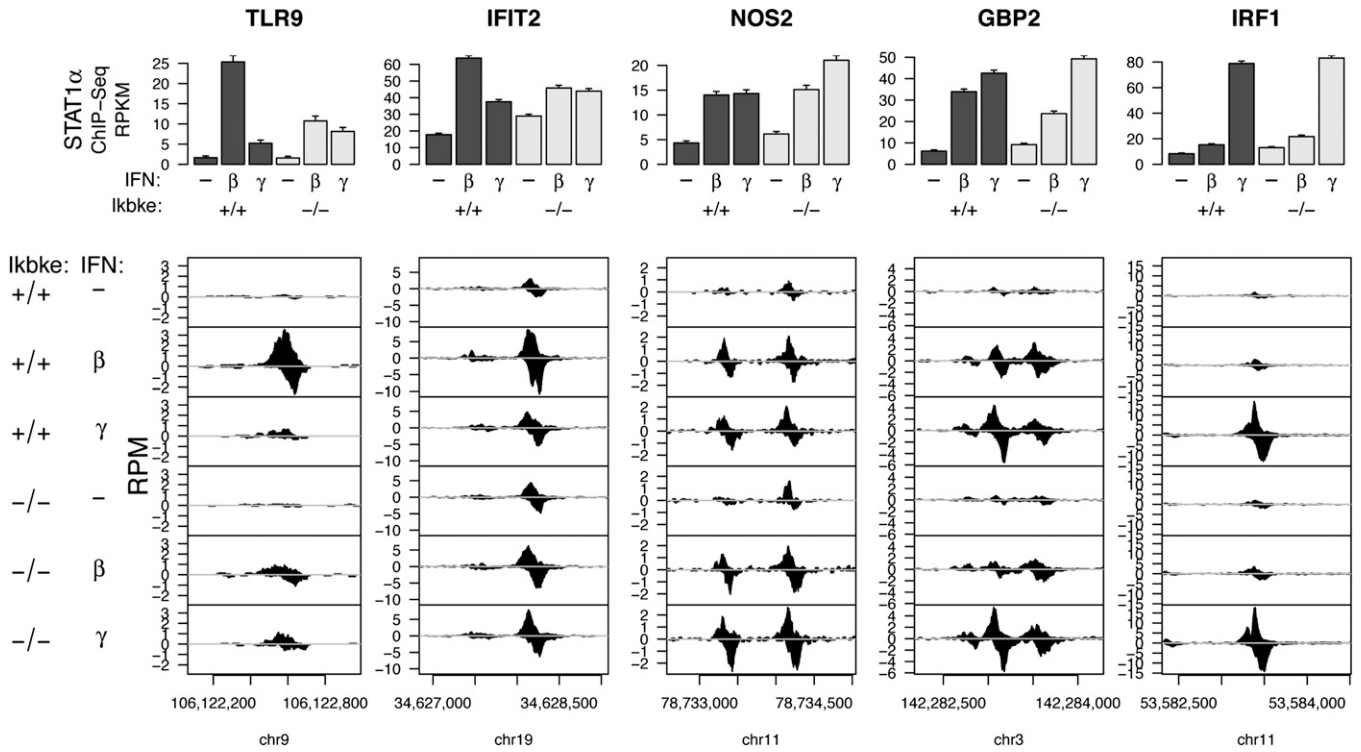

Fig. S7. Binding of STAT1α to the promoters of ISGs during IFN stimulation in bone marrow-derived macrophages. Peaks called by MACS (1) relative to ChIP input controls are shown. (*Upper*) ChIP-seq RPKM values for peaks associated with representative ISGs. (*Lower*) Normalized ChIP-seq reads across the gene-associated region (units are RPM, or "reads per million"—the number of reads overlapping a given position divided by the total number of aligning reads in each sample, in millions).

1. Zhang Y, et al. (2008) Model-based analysis of ChIP-Seq (MACS). *Genome Biol* 9:R137.